Coarse graining of elastic interactions under 20 MeV

(Nucleon alpha scattering)

June 2019

Aurora Ortega Moral

Supervisors: Enrique Ruiz Arriola, Ignacio Luis Ruiz Simó.

Department of Atomic, Nuclear and Molecular Physics, UGR

Inter-University Master's Degree in Nuclear Physics
University of Sevilla

UNIVERSIDAD
DE GRANADA

Contents

1 Introduction

In a scattering experiment we make two particles to collide at different energies and study the result of that collision to obtain information about the interaction. Scattering has always been an important tool since Rutherford discovered the nucleus in 1911 using a beam of α particles and a thin gold foil target. Almost everything we know about nuclear and atomic physics has been explained using these kind of experiments.
Scattering a beam of particles off a target allows us to obtain the so-called cross section that measures the relation between collision frequency and projectile incident flux; then phase shifts, another very important scattering parameters can be calculated. Theses phase shifts contain information about strength and functional dependence of the potential V acting between the projectile and the target particle. The theoretical tool used to explain scattering experiments is scattering theory.

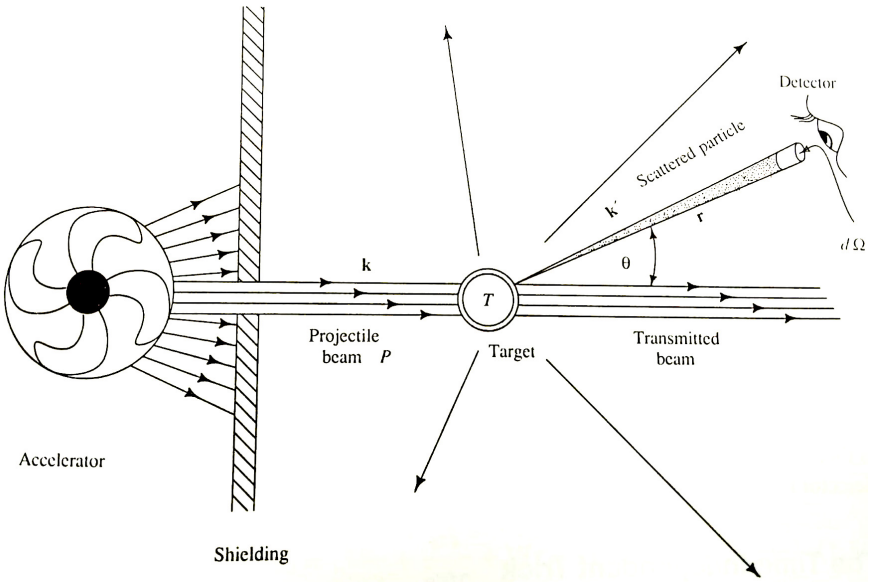

Figure 1: Scattering schedule.(Image Rubin Landau [1]).

As a result of collisions, several outcomes are possible depending mainly on the beam energy. We may then study separately different processes. See introduction of Ref [2].

$$A + B \rightarrow \begin{cases} A + B, & \text{elastic} \\ A + B^* & \text{inelastic} \\ A + B^* + C & \text{inelastic} \\ C & \text{absorption} \end{cases}$$

Each of these possibilities is known as a channel. In general, the scattering process is multichannel, but it sometimes happens that most of them are closed due to energy considerations. For example if the beam energy is low enough then only the elastic channel is open. As the energy increases new channels will open up. In this work the $n - \alpha$ and $p - \alpha$ scattering processes are going to be studied. We will set the incident particle energies below 20 MeV, so only elastic scattering is going to be considered.

As we said, scattering theory tries to get an interaction potential including all important information about it. Several potential models have been studied over the last years. Some models studying our same energy ranges are for example "An optical model for the scattering of nucleons from ^4He bellow 20 MeV " [7] or "Refinement of the $n-\alpha$ and $p-\alpha$ fish bone potential" [8]. We are going to use the first one to build up our own method and reproduce their main results.
These potential models are continuous functions with some parameters that have been fitted to experiments. The approximation model proposed in this work uses a grained potential composed by N square wells.The physical parameters in this model are the depth of each small square well shaping the full potential. We aim to understand how many of them are actually necessary. As we will see, a very good approximation is achieved with a considerably small number of square wells if we allow to fit the strengths of the square well potential to the data.
First, we are going to mathematically develop this method reproducing important results of differential cross sections and phase shifts using as our square well depths the ones predicted by the Optical potential approximation. Then we leave our parameters free and find their values after a minimization process using experimental data.
In this work, we will review Scattering theory highlighting relevant parts of the study. The contents of this work are summarized as follows. First, we describe Schrödinger scattering equation and its solution (Section 3), we introduce important scattering parameters such as cross section and polarization in Section 4, that are going to connect experiments and theory. Then Spin-Orbit interaction (Section 5) and also Coulomb interaction for charged particles (Section 6) are taken into account. Once we have the theoretical tools we develop the graining method using the Optical continuous potential model in Section 7, solve Schrödinger equation for each well, join solutions and get important scattering information as phase shifts, differential cross sections and polarizations (Section 8). Once we have built mathematically our solution method we may be able to minimize parameters of the theoretical potential directly with experimental data (Section 9). Finally, in order to obtain confidence intervals of the obtained results we use a Monte Carlo Simulation in Section 10.

Several sources have been consulted while writing and developing this work, they are all included in the bibliography, but the help of Rubin Landau (Quantum Mechanics II) book [1] should be highlighted.

2 Scattering description

In scattering theory it is convenient to recognize various possible characteristics of the problem: relativistic and non-relativistic case, single-channel scattering or multi-channels scattering and time-dependent or independent. In the present report we are going to study heavy particles at low energies, from 0 to 20 MeV. This choice allows us to make the non-relativistic approximations and also assume single-channel scattering.
We describe time-dependent scattering using wave packets. The one for the entire system is the sum of incident and scattered wave packets (see Rubin Landau [1]).

$$\Psi(\vec{r},t) = \phi_k(\vec{r},t) + \Psi_k^{SC}(\vec{r},t). \tag{1}$$

If we imagine a plane wave continuously entering along the axis instead of a wave packet, each term would have the stationary-state time dependence (e^{-iE_kt}) which can be factored out, getting the time-independent approximation:

$$\Psi(\vec{r}) = \phi_k(\vec{r}) + \Psi_k^{SC}(\vec{r}). \tag{2}$$

Where the incident plane wave packet $\phi_k(\vec{r})$ is defined:

$$\phi_k(\vec{r}) = \int d^3k e^{i\vec{k}\cdot\vec{r}} A_{k_0}(\vec{k}) \tag{3}$$

Where A_{k_0} is a peaked function around the beam momentum k_0.
The scattered part is analogously defined as:

$$\Psi_k^{SC}(\vec{r}) = \int d^3k \frac{e^{i\vec{k}\cdot\vec{r}}}{r} A_{k_0}(\vec{k}) F(\vec{k},\hat{r}) \tag{4}$$

Where $\hat{r}$ is the unit vector along the direction of the observed scattered wave and $F(\vec{k},\hat{r})$ is a function describing the strength and the angular dependence of the scattering. Assuming the outgoing wave packet will remain sharp and spreading slowly this function can be considered to be sharp around the beam momentum k_0 so it can be factored out of the integral. The full wave function has the asymptotic form at $r \to \infty$:

$$\Psi(\vec{r}) \sim N\left[e^{ikz} + f_E(\theta,\phi)\frac{e^{ikr}}{r}\right] \tag{5}$$

Where $f_E(\theta,\phi)$ is the so-called scattering amplitude defined as $F(\vec{k},\hat{r})$ evaluated at k_0. The first term of previous equation corresponds to the incident plane wave and the second one to the scattered spherical one, both normalized. This scattering wave function $\Psi(\vec{r})$ is the solution of the time-independent Schrödinger equation.

3 Schrödinger equation

3.1 2-Body Schrödinger equation

Scattering dynamics is determined by the 2-particles Schrödinger equation and in our specific case, the time-independent one,

$$H_{\text{tot}}\,\psi(\vec{r}_1,\vec{r}_2) = E_{tot}\,\psi(\vec{r}_1,\vec{r}_2). \tag{6}$$

This 2-body problem can be reduced to two separate, effective 1-body problems by changing variables. We then get an equation that describes the CM's motion:

$$\frac{p_{CM}^2}{2M_T}\,\phi_{CM}(\vec{R}) = E_{CM}\,\phi_{CM}(\vec{R}) \tag{7}$$

and another one describing the relative motion of the two particles:

$$\left[\frac{p^2}{2\mu} + V(r)\right]\Psi(\vec{r}) = E\Psi(\vec{r}) \tag{8}$$

Where $\vec{r}$ is the relative position of particles $\vec{r} = \vec{r_1} - \vec{r_2}$, $\vec{R}$ is the position of their center of mass and $\mu = \frac{M_1 M_2}{M_1+M_2}$ is the reduced mass. Equation (7) is just the familiar plane wave one. The CM of the system moves like a free particle. We are mainly going to solve the relative wave function in the CM frame, Equation (8), throughout this work.

3.2 Relative motion Schödinger equation. Partial wave Expansion.

Assuming a central potential and rewriting $\Psi(\vec{r})$ in polar coordinates, we can write the wave function as a linear combination of partial waves ψ_{lm}. This is the so-called partial wave expansion.

$$\Psi(\vec{r}) = \sum_{l,m} 4\pi i^l \frac{u_l(kr)}{kr} Y_{lm}(\hat{r}) \frac{Y_{lm}^*(\hat{k})}{(2\pi)^{3/2}} \tag{9}$$

This infinite sum can be truncated. When increasing the orbital momentum value l, the distortion of the scattered-wave becomes smaller up to a maximum value of the orbital momentum l_{max} from which the wave function is no longer influenced by the interaction, becoming again a plane wave. This value can be approximated as $l_{max} = ka_N$ where a_N is the potential range and k the free particle momentum.

Using the spherical harmonics addition theorem, Equation (9), can we written as:

$$\Psi(\vec{r}) = \sum_{l=0}^{\infty} i^l \frac{u_l(kr)}{kr}(2l+1)\frac{P_l(\cos\theta)}{(2\pi)^{3/2}} \tag{10}$$

Those partial wave functions in the sum are composed by an angular and a radial part:

$$\psi_{lm}(\vec{r}) = R_l(kr)Y_{lm}(\theta,\phi), \tag{11}$$

The angular part $Y_{lm}(\theta,\phi)$ is described by the spherical harmonics functions. They are eigenfunctions of $\vec{L^2}$ and L_z. The radial wave function $R_l(r)$ is determined by the radial equation:

$$\left[\frac{p_r^2}{2\mu} + \frac{l(l+1)}{2\mu r^2}\hbar^2 + V(r)\right] R_l(kr) = ER_l(kr). \tag{12}$$

The left-hand side of the Hamiltonian represents the radial kinetic energy while the second is the rotational kinetic energy acting as a repulsive potential (centrifugal barrier) where l is the eigenvalue of orbital angular momentum and p_r operator is $p_r \equiv -i\hbar\frac{1}{r}\frac{\partial}{\partial r}r$.

Multiplying by $2\mu/\hbar^2$, introducing new variables $U(r) = 2\mu V(r)/\hbar^2$, $\varepsilon = 2\mu E/\hbar^2$ and using natural units $\hbar = c = 1$ we get to the radial equation

$$\frac{\mathrm{d}^2 R_l}{\mathrm{d}r^2} + \frac{2}{r}\frac{\mathrm{d}R_l}{\mathrm{d}r} + \left[\varepsilon - U(r) - \frac{l(l+1)}{r^2}\right] R_l = 0 \tag{13}$$

also, it is convenient to make the following substitution :

$$u_l(kr) \equiv rR_l(kr) \tag{14}$$

where $u_l(r)$, the reduced radial function, satisfies the reduced radial equation for the partial wave l:

$$H_l u_l = -u_l'' + \left[\frac{l(l+1)}{r^2} + U(r)\right] u_l = \varepsilon u_l \tag{15}$$

Reordering terms and using $E = K^2/2\mu$ relation makes us rewrite the previous equation more compactly as:

$$-u_l'' + \left(\frac{l(l+1)}{r^2} + U(r) - K^2\right) u_l = 0 \tag{16}$$

3.3 Reduced radial equation solution

The general solution of (16) for $U(r) = U_0$ is a linear combination of first $j_l(kr)$ and second kind $n_l(kr)$ spherical Bessel functions

$$u_l(kr) = Akrj_l(kr) - Bkrn_l(kr) \tag{17}$$

where k value is defined $k = (-U_0 + K^2)^{1/2}$. We have to take into account two different situations in order to solve the equation: $r > a_R$ where $U(r) = 0$ and $r < a_N$, being a_N the potential range. Also introducing the reduced spherical Bessel functions $krj_l(kr) = \hat{j}_l(kr)$ and $-krn_l(kr) = \hat{n}_l(kr)$ we may rewrite Equation (17) as:

$$u_l(kr) = A\hat{j}_l(kr) + B\hat{n}_l(kr) \tag{18}$$

Solution at $r < a_N$

The solution of the wave function has to be regular at $r = 0$. The reduced spherical Bessel functions when $r \to 0$ take the limit. See Galindo & Pascual [4]:

$$\begin{aligned} \hat{j}_l(x) &= \frac{(x)^{l+1}}{(2l+1)!!} \\ \hat{n}_l(x) &= \frac{(2l-1)!!}{x^l} \end{aligned} \tag{19}$$

We get from these behaviors that $B = 0$ since $u_l(k_1 r)$ must be regular at the origin and $n_l(0)$ term diverges. Then we obtain:

$$u_l(k_1 r) = A\hat{j}_l(k_1 r) \tag{20}$$

Where $k_1 = \sqrt{K^2 - U_0}$

Solution at $r > a_N$

In this case the potential $U(r) = 0$ and $k_2 = K$

$$u_l(k_2 r) = C\hat{j}_l(k_2 r) + D\hat{n}_l(k_2 r) \tag{21}$$

In the $r \to \infty$ limit, $\frac{l(l+1)}{r^2} \to 0$. The solution is the free particle one plus a phase shift $\delta_l(E)$.

$$u_l(r \to \infty) = \sin(kr - \frac{l\pi}{2} + \delta_l(E)) \tag{22}$$

This phase shift contains information about the scattering process. It can be interpreted as the influence of the potential at large distances, that translates into a shifted solution of the free particle one by the quantity $\delta_l(E)$. Note, by definition, that it depends on the potential but also depends on the particle energy. We are going to leave aside this energy dependence in equations for simplicity. Reduced spherical Bessel functions when $r \to \infty$ take the form

$$\hat{j}_l(x) = \sin\left(x - \frac{l\pi}{2}\right) \quad , \quad \hat{n}_l(x) = \cos\left(x - \frac{l\pi}{2}\right) \tag{23}$$

then the solution $u_l(kr)$ at $r \to \infty$ states

$$u_l(kr) = C\sin\left(kr - \frac{l\pi}{2}\right) + D\cos\left(kr - \frac{l\pi}{2}\right) \tag{24}$$

We can rewrite the sine of two angles sum using the trigonometric identity:

$$\sin\left(kr - \frac{l\pi}{2} + \delta_l(E)\right) = \sin\left(kr - \frac{l\pi}{2}\right)\cos(\delta_l) + \cos\left(kr - \frac{l\pi}{2}\right)\sin(\delta_l) \tag{25}$$

Comparing this expression with the previous one we identify $C = \cos(\delta_l)$ and $D = \sin(\delta_l)$. Then the general solution in the $r > a_R$ case is given by

$$u_l(k_2 r) = \cos(\delta_l)\hat{j}_l(k_2 r) + \sin(\delta_l)\hat{n}_l(k_2 r) \tag{26}$$

4 Important Scattering parameters

4.1 Phase Shifts

As we said in previous section, the phase shift is a really important variable since it carries all scattering process information and allow us to calculate all the important scattering observables (Galindo Pascual Scattering theory) [3]. The phase shift δ_l is calculated using the continuity of the wave function at $r = a_N$. This condition is easily set by imposing continuity on $u_l(kr)$ and its derivative $u_l'(kr)$. Both of them can be calculated simultaneously evaluating the logarithmic derivative:

$$\mathscr{L}(r = a_N) \equiv \left.\frac{\mathrm{d}u_l(kr)/\mathrm{d}r}{u_l(kr)}\right|_{r=a_N} \tag{27}$$

Defining $u_1(k_1 r)$ as the solution at $r < a_N$ and $u_2(k_2 r)$ the other for the $r > a_N$ case, we may calculate:

$$\left.\frac{u_1'(k_1 r)}{u_1(k_1 r)}\right|_{r=a_N} = \left.\frac{u_2'(k_2 r)}{u_2(k_2 r)}\right|_{r=a_N} \tag{28}$$

Where u_n' is defined as $u_n' = \frac{du_n(kr)}{dr}$. Substituting $u_1(k_1 r)$, $u_2(k_2 r)$ and their derivatives:

$$\frac{\hat{j}_l'(k_1 a_R)}{\hat{j}_l(k_1 a_R)} = \frac{\cos(\delta_l)\hat{j}_l'(k_2 a_R) + \sin(\delta_l)\hat{n}_l'(k_2 a_R)}{\cos(\delta_l)\hat{j}_l(k_2 a_R) + \sin(\delta_l)\hat{n}_l(k_2 a_R)} \tag{29}$$

Dividing by $\cos(\delta_l)$ both numerator and denominator of the right-hand side term and defining $\mathscr{L} = \frac{\hat{j}_l'(k_1 a_R)}{\hat{j}_l(k_1 a_R)}$, the phase shift can be calculated as:

$$tan(\delta_l) = \frac{\mathscr{L}\hat{j}_l(k_2 a_R) - \hat{j}_l'(k_2 a_R)}{\hat{n}_l'(k_2 a_R) - \mathscr{L}\hat{n}_l(k_2 a_R)} \tag{30}$$

From the δ_l definition, we can calculate theoretically the most important observables of an scattering experiment: scattering amplitude, differential cross section and total cross section.

4.2 Scattering amplitude

The scattering amplitude is the main experimental observable in scattering theory, it is usually defined as the sum:

$$f(\theta) = \sum_{l=0}^{\infty}(2l+1)P_l(\cos(\theta))\frac{\eta_l e^{2i\delta_l} - 1}{2ik}. \tag{31}$$

Where $P_l(\cos(\theta))$ are the Legendre polynomials and η_l is a parameter that includes information about the elasticity of the process. We are considering pure elastic scattering (no absorption), then in our case $\eta_l = 1$.

4.3 Differential cross section

Differential cross section for elastic scattering $\frac{d\sigma}{d\Omega}$ is a function that quantifies the intrinsic rate at which the scattered projectiles can be detected at a given angle (θ, ϕ) with respect to the beam direction and subtending a solid angle $d\Omega$. It is defined:

$$\frac{d\sigma}{d\Omega} = \lim_{\Delta \to 0} \frac{N(\theta, \phi)/\Delta\Omega}{N_{in}/\Delta A_{in}} \tag{32}$$

Differential cross section is a quantity independent of detector size, beam current and size of the target. The total number of scattered particles $N(\theta, \phi)$ within the subtended solid angle $\Delta\Omega$ is divided by the relation between the total number of incident particles N_{in} and the unit area of the target ΔA_{in}, orthogonal to the beam. Then the limit for infinitesimally small detector size and thin targets is taken.
Dividing by a time interval Δt, taking the limit $\Delta t \to 0$ to get currents we arrive to the relation of scattering amplitude and differential cross section.

$$\frac{d\sigma}{d\Omega} = \mid f_E(\theta, \phi) \mid^2 \frac{v_{out}}{v_{in}} \tag{33}$$

If scattering incident and outgoing velocities are equal $\left(\frac{v_{out}}{v_{in}} = 1\right)$ and also in our particular case forces are central, then scattering is axially symmetric and does not depend on ϕ $(f_E(\theta, \phi) = f_E(\theta))$. Thus equation (33) can be simplified:

$$\frac{d\sigma}{d\Omega} = \mid f_E(\theta) \mid^2 \tag{34}$$

The differential cross section has the dimension of area per solid angle.

4.4 Total cross section

The total cross section is a scalar magnitude with area units. It measures the relation between collision frequency and projectile incident flux. It is defined as the integration all over different scattering angles of the differential cross section.

$$\sigma_t(E) = \int d\Omega \left(\frac{d\sigma_{el}}{d\Omega} + \frac{d\sigma_{ne}}{d\Omega} \right) \tag{35}$$

In the present case (elastic process) $\sigma_t = \sigma_{el}$

$$\sigma_{el}(E) = \int d\Omega \frac{d\sigma}{d\Omega}(\theta, \phi) \tag{36}$$

Total cross section is a very important observable since it is much more easy to measure than differential cross section. It is related to the scattering amplitude by the Optical Theorem:

$$\sigma_t = \frac{4\pi}{k} Im f_E(0^o) \tag{37}$$

5 Scattering with spin-orbit Potential

Scattering theory for spin particles differs from the spinless theory just in one respect: There is a large number of possible amplitudes and cross sections, one of them for every choice of initial and final spin states.

The Hilbert space for particles with spin is more complicated and the Hamiltonian is spin-dependent containing terms such as the spin-orbit interaction. Since V is invariant under rotations (space's isotropy), it may contain a central term V_c (function of k, k' and r and other scalar pieces under global rotations. See Rubin Landau [1] for further details.

$$V_N = V_c + V_a \vec{s}\cdot\vec{k} + V_b \vec{s}\cdot\vec{k'} + V_s \vec{s}\cdot(\vec{k}\times\vec{k'}) \tag{38}$$

Usually, we call $\hat{\mathbf{n}} = \frac{\vec{k}\times\vec{k'}}{|\vec{k}\times\vec{k'}|}$

The surviving terms after imposing V to be invariant under time reversal and parity transformation is just the scalar product of the two $\vec{s}$ and $\hat{n}$ axial vectors. Then, the potential with spin dependence states:

$$V_N = V_c + V_s \vec{s}\cdot\hat{n} \tag{39}$$

usually written in coordinate representation:

$$V = V_c(r) + V_s(r)\,\vec{s}\cdot\vec{l} \tag{40}$$

The solution of Schrödinger equation is the same that the one for spinless particles. In both cases, one expects V will fall off to zero as the two particles move apart. Thus, we expect V_s going to zero rapidly and we can still impose the same asymptotic conditions at $r \to \infty$. Schrödinger equation splits into two, uncoupled one-dimensional, differential equations. Now each one for a state of different j: $u_l^{(+)}$ for $j = l + \frac{1}{2}$ and $u_l^{(-)}$ for $j = l - \frac{1}{2}$.

$$\left[\frac{-1}{2\mu}\frac{d^2}{dr^2} + \frac{l(l+1)}{2\mu r^2} + V_c(r) + \frac{l}{2}V_s(r)\right] u_l^{(+)}(kr) = E u_l^{(+)}(kr) \tag{41}$$

$$\left[\frac{-1}{2\mu}\frac{d^2}{dr^2} + \frac{l(l+1)}{2\mu r^2} + V_c(r) - \frac{(l+1)}{2}V_s(r)\right] u_l^{(-)}(kr) = E u_l^{(-)}(kr) \tag{42}$$

As we mentioned above, the main difference compared to spinless theory cases comes when calculating the values of the observables (scattering amplitude, differential cross section and total cross section). When we have particles with spin there are multiple choices of initial and final states and also experimental different conditions that modify the obtained results.

Scattering amplitude

We may distinguish two possible scattering amplitudes for each u_l corresponding to the two possible solutions (values of j for a given l except for $l = 0$). When decomposing the distorted-wave in partial wave expansion and applying the boundary conditions at large distances we see that, for a given initial spin, the scattered wave has a part with spin up and another one has been flipped to down [1]. For example, distorted (initially spin up)-wave $\left(u_l^{(+)}\right)$ has the form:

$$\psi_\uparrow(\vec{r}) \sim \phi_\uparrow(\vec{r}) + \frac{e^{ikr}}{r}\frac{f_{++}(\theta)\,|\uparrow\rangle + f_{-+}(\theta)\,|\downarrow\rangle}{(2\pi)^{3/2}} \tag{43}$$

Here we have introduced the *spin-nonflip amplitude* and the *spin-flip amplitude* defined in terms of the phase shifts δ_l^+ and δ_l^- defined for $j = l + \frac{1}{2}$ case and $j = l - \frac{1}{2}$, respectively.

$$f(\theta) = f_{++}(\theta) = \sum_{l=0}^{\infty} \frac{1}{k} \left[(l+1) e^{i\delta_l^+} \sin\delta_l^+ + l e^{i\delta_l^-} \sin\delta_l^- \right] P_l(x) \tag{44}$$

$$g(\theta) = -\frac{f_{-+}(\theta,\phi) e^{-i\phi}}{\sin\theta} \tag{45}$$

this latter equation leads to the simpler form:

$$g(\theta) = \frac{1}{k} \sum_{l=1}^{\infty} \left[e^{i\delta_l^+} \sin(\delta_l^+) - e^{i\delta_l^-} \sin\delta_l^- \right] \frac{dP_l(x)}{dx} \tag{46}$$

We may write spin up to spin down amplitude (f_{-+}) and spin down to spin up one (f_{+-}) as a function of $g(\theta)$.

$$f_{-+} = -e^{i\phi} \sin\theta g(\theta) \tag{47}$$

$$f_{+-} = e^{-i\phi} \sin\theta g(\theta) \tag{48}$$

and

$$f_{++} = f_{--} \tag{49}$$

Cross Sections

The definition of cross section is still the same as in the spinless scattering, namely as the square of the scattering amplitudes. The problem is that amplitude depends on the initial spin state and also on the experiment itself, obtaining different cross section values depending upon whether the spin of the final state is observed or not. If the incident beam has spin up and the scattered one is observed to be up, then the cross section is:

$$\frac{d\sigma}{d\Omega}(\uparrow\Leftarrow\uparrow) = \left.\frac{d\sigma}{d\Omega}\right|_{non-flip} = |\langle\uparrow|\mathscr{F}|\uparrow\rangle|^2 = |f_{++}|^2 = |f(\theta)|^2 \tag{50}$$

Where we can use an operator $\mathscr{F}$ in spin space (square matrix of two dimensions) which is oftenly used to express spin dependence in an easier way, taking the suitable elements in each case. Analogously, the cross section of a spin-down incident beam and spin-down observed scattered one is:

$$\frac{d\sigma}{d\Omega}(\downarrow\Leftarrow\downarrow) = \left.\frac{d\sigma}{d\Omega}\right|_{non-flip} = |\langle\downarrow|\mathscr{F}|\downarrow\rangle|^2 = |f_{--}|^2 = |f(\theta)|^2 \tag{51}$$

If the incident beam is known to have well-defined spin and scattered one is measured and it has its spin flipped, then

$$\frac{d\sigma}{d\Omega}(\downarrow\Leftarrow\uparrow) = \left.\frac{d\sigma}{d\Omega}\right|_{flip} = |\langle\downarrow|\mathscr{F}|\uparrow\rangle|^2 = |f_{-+}|^2 = \sin^2(\theta)|g(\theta)|^2 \tag{52}$$

The other possibility:

$$\frac{d\sigma}{d\Omega}(\uparrow\Leftarrow\downarrow) = \left.\frac{d\sigma}{d\Omega}\right|_{flip} = |\langle\uparrow|\mathscr{F}|\downarrow\rangle|^2 = |f_{+-}|^2 = \sin^2(\theta)|g(\theta)|^2 \tag{53}$$

In the case we know initial spin state i ($i = +, -$) but the scattered beam spin is not observed, we have to add probabilities for scattering to spin up and down:

$$\begin{aligned}\frac{d\sigma}{d\Omega}(? \Leftarrow i) = \left.\frac{d\sigma}{d\Omega}\right|_{flip} + \left.\frac{d\sigma}{d\Omega}\right|_{non-flip} = \\ = |\langle\uparrow|\mathscr{F}|i\rangle|^2 + |\langle\downarrow|\mathscr{F}|i\rangle|^2 = \\ = |f_{-ii}|^2 + |f_{ii}|^2 = \sin^2(\theta)|g(\theta)|^2 + |f(\theta)|^2\end{aligned} \tag{54}$$

If an initial beam is in one concrete spin state i it is because it has been polarized with a polarization $\vec{P_i}$.
$\vec{P_i}$ is defined as the normalized expectation value of the spin:

$$\vec{P_i} = \frac{\langle\chi_i|\vec{\sigma}|\chi_i\rangle}{\langle\chi_i|\chi_i\rangle} \tag{55}$$

Any $|\chi_i\rangle$ state can be written as a linear combination of spin up and spin down states:

$$|\chi_i\rangle = \alpha_+ \,|\uparrow\rangle + \alpha_- \,|\downarrow\rangle \tag{56}$$

Polarization in state χ_i is then given by:

$$\begin{aligned}\vec{P_i} = \langle\chi_i|\vec{\sigma}|\chi_i\rangle = \\ = 2\Re\,(\alpha_+^*\alpha_-)\hat{e_x} + 2\Im\,(\alpha_+^*\alpha_-)\hat{e_y} + (|\alpha_+|^2 - |\alpha_-|^2)\hat{e_z}\end{aligned} \tag{57}$$

We can write equation cross section introducing polarization concept:

$$\begin{aligned}\frac{d\sigma}{d\Omega}(? \Leftarrow i) = \sum_{\chi_f=\uparrow,\downarrow} |\langle\chi_f|\mathscr{F}|\chi_i\rangle|^2 = \\ \sin^2(\theta)|g(\theta)|^2 + |f(\theta)|^2 + 2\vec{P_i}\cdot\hat{n}\sin\theta\,\Im\left[g(\theta)^* f(\theta)\right]\end{aligned} \tag{58}$$

In our particular study we consider non-polarized beams, so the average value of $\vec{P} = 0$ is zero and we have no contribution of the last factor in Equation 59. We may go back to equation (54).
In order to obtain the polarization of the scattered particle, we define the scattered spin state:

$$|\chi_f\rangle = \mathscr{F}\,|\chi_i\rangle \tag{59}$$

Using the polarization definition, Equation (55) and substituting this $|\chi_f\rangle$ and $\mathscr{F}$ expressions, we get to the equation, for the particular case where the initial beam is unpolarized:

$$P_f(f \Leftarrow 0) = \frac{2\ \Im[g(\theta)^* f(\theta)\sin(\theta)]}{|f(\theta)|^2 + |g(\theta)|^2\sin^2(\theta)} \tag{60}$$

6 Coulomb force. Charged particles.

We are going to calculate scattering parameters also for charged particles (protons). Then we may introduce Coulomb's force between particles. This part of the interaction is described by the Coulomb Potential from an uniformly charged sphere of radius R_C:

$$V_C(r) = \begin{cases} \frac{1}{4\pi\epsilon_0}\frac{e^2}{R_C}\left(3 - \frac{r^2}{R_C^2}\right) & r < R_C \\ \frac{1}{4\pi\epsilon_0}\frac{2e^2}{r} & r > R_C \end{cases} \tag{61}$$

So, in this case the total potential is given by:

$$V_T = V_N + V_C \tag{62}$$

Radial equation including Coulomb potential is written:

$$-u_l^{''} + \left(\frac{l(l+1)}{r^2} + 2\mu(V_N + V_C) - K^2\right) u_l = 0 \tag{63}$$

In the particular case $r > R_C : V_N = 0$ equation 63 can be written as:

$$u_l^{''} + \left(1 - \frac{2\eta}{\rho} - \frac{l(l+1)}{\rho^2}\right) u_l = 0 \tag{64}$$

Where we have divided by K^2 , used $\rho = Kr$ variable and introduced the Coulomb parameter $\eta = \frac{\mu Z_p Z_T e^2}{K}$

The general solution of Equation (63) at $r < R_C$ is mainly the same as the non-charged equation solution, Equation (16), just introducing a new adding term in the potential function. The problem comes when solving for $r > R_C$. The solution of the reduced radial function may differ from the non-charged particle one since now we cannot make the approximation of potential set to 0 at $r \to \infty$. The Coulomb potential term does not vanish faster enough for large distances so the solution is not the same as for short-range potentials.
We may introduce Coulomb wave-functions $F_l(\eta, \rho)$ and $G_l(\eta, \rho)$ as the two linearly independent solutions of the new differential equation. Most important properties for us are the $r \to 0$ and $r \to \infty$ behaviors:

$$\begin{aligned} F_l(\eta,\rho) &= \begin{cases} \rho^{l+1}, & \text{for } \rho \to 0 \\ \sin[\rho - \eta ln(2\rho) - l\pi/2 + \sigma_l], & \text{for } \rho \to \infty \end{cases} \\ G_l(\eta,\rho) &= \begin{cases} \rho^{-l}, & \text{for } \rho \to 0 \\ \cos[\rho - \eta ln(2\rho) - l\pi/2 + \sigma_l], & \text{for } \rho \to \infty \end{cases} \end{aligned} \tag{65}$$

Where σ_l are the so-called Coulomb phase shifts. They measure how much $F_l(\eta, \rho)$ and $G_l(\eta, \rho)$ phases are shifted from free waves. The same theory is still applicable: ψ still decomposes into incident plus scattered waves. These waves now are distorted also by the long range Coulomb potential but scattering observables are defined in terms of currents so these are unaffected by

phase factors. If $\eta = 0$, Coulomb waves reduce to the previous neutral charge free scattering case:

$$\begin{aligned} F_l(\eta = 0, \rho) &= \hat{j}_l(\rho) \\ G_l(\eta = 0, \rho) &= +\hat{n}_l(\rho) \end{aligned} \tag{66}$$

A subroutine made by L.L.Salcedo using I.J.THOMPSON ([10]) has been used in order to calculate the solution at $r > R_C$ in the specific case of charged particles.

7 Potential graining

Our method in order to calculate different scattering observables is based on a grained description of the potential. This method has been developed and used by F.S Pedro, R.Navarro Pérez, J.E. Amaro and E.Ruiz Arriola ([6], [13], [14] and [15]). In this way, we can split the problem into solving some Schrödinger equations of small square wells equally-spaced from 0 to a_N. In the process of developing the graining method we take concrete potential values for each small well obtained by evaluating the optical potential function, Equation (38) at the center of each of them. Then setting the continuity of the solution in the transition points we will calculate phase shifts. Finally, using phase shifts we can easily calculate the rest of the observables. The interaction as we have said is built as a sequence of square wells, the radial component of the potential (non-charged particles case) stands:

$$V(r) = \begin{cases} V_1 & 0 \leq r < a_1 \\ V_2 & a_1 \leq r < a_2 \\ ... & \\ V_i & a_{i-1} \leq r < a_i \\ ... & \\ V_N & a_{N-1} \leq r < a_N \\ 0 & r \geq a_N. \end{cases} \tag{67}$$

We are going to use this potential to solve the Schrödinger equation

$$-u_l^{''} + \left(\frac{l(l+1)}{r^2} + U(r) - K^2 \right) u_l = 0 \tag{68}$$

Solutions in each small well are given

$$u_{ln}(r) = \begin{cases} u_{l1}(k_1 r) = A\hat{j}_l(k_1 r) & 0 \leq r < a_1 \\ u_{l2}(k_2 r) = \cos(\delta_1)\hat{j}_l(k_2 r) + \sin(\delta_1)\hat{n}_l(k_2 r) & a_1 \leq r < a_2 \\ ... & \\ u_{li}(k_i r) = \cos(\delta_{i-1})\hat{j}_l(k_i r) + \sin(\delta_{i-1})\hat{n}_l(k_i r) & a_{i-1} \leq r < a_i \\ ... & \\ u_{lN}(k_N r) = \cos(\delta_{N-1})\hat{j}_l(k_N r) + \sin(\delta_{N-1})\hat{n}_l(k_N r) & a_{N-1} \leq r < a_N \\ u_{lf}(Kr) = \cos(\delta_N)\hat{j}_l(Kr) + \sin(\delta_N)\hat{n}_l(Kr) & r \geq a_N. \end{cases} \tag{69}$$

Where:

$$k_i = \sqrt{K^2 - 2\mu V_i} = \sqrt{K^2 - U_i} \tag{70}$$

We may impose continuity of the solution at points a_n, imposing continuity of the logarithmic derivative:

$$\mathscr{L}_n(r = a_n) \equiv \left. \frac{\mathrm{d}u_{ln}(r)/\mathrm{d}r}{u_{ln}(r)} \right|_{r=a_n} = \left. \frac{\mathrm{d}u_{l(n+1)}(r)/\mathrm{d}r}{u_{l(n+1)}(r)} \right|_{r=a_n}, \tag{71}$$

Once we obtain δ_1 solving the previous equation when $r = a_1$, we can obtain the rest of phase shift recursively. The total one δ_N is called the accumulated phase shift. The general expression for any δ_n is given by:

$$\delta_n = tg^{-1} \left(\frac{\mathscr{L}_n \hat{j}_l(k_{n+1}a_n) - \hat{j}_l'(k_{n+1}a_n)}{\hat{n}_l{}'(k_{n+1}a_n) - \mathscr{L}_n \hat{n}_l(k_{n+1}a_n)} \right) \tag{72}$$

The only change that we have to make when dealing with the charged particle case is to introduce an extra potential term when $r < a_N$ corresponding to the Coulomb force and, most important, to replace the solution of the wave function at $r > a_N$ being in this case built by the previously introduced Coulomb wave functions, Equation (66). This last solution outside the potential will be described:

$$u_{lf}(Kr) = \cos(\delta_N)F_l(Kr) + \sin(\delta_N)G_l(Kr) \qquad r \geq a_N. \tag{73}$$

7.1 Reproduced Potential

The total potential $V_T(r)$ is considered real because we stay below the inelastic threshold under the energies considered in this work. Also it includes a central term $V_c(r)$, the Coulomb interaction one $V_C(r)$ and the spin-orbit $V_{s-o}(r)$ factor.

$$V_T(r) = V_N(r) + V_C(r) \tag{74}$$

$$V_T(r) = V_c(r) + V_{s-o}(r) + V_C(r) \tag{75}$$

In equation 74, $V_C(r)$ is the Coulomb potential from an uniformly charged sphere of radius R_C described in previous section while V_N is the non charged (neutral) part of the potential. The potential equation (76) was proposed by G.R.Satchler and L.W.Owen [7] and their obtained fitting parameters in equations (79) and (80) are used to give values to our potential wells depths by evaluating the function in the center of each of them.

$$V_N(r) = -V(e^x + 1)^{-1} + (\hbar/m_\pi c)^2 V_s \vec{L} \cdot \vec{\sigma} r^{-1}(d/dr)(e^{x_s} + 1)^{-1} \tag{76}$$

This potential $V_N(r)$ has the Woods-Saxon form, with a spin-orbit coupling term that has the Thomas form but which is allowed to have parameters differing from those of the central potential. We can distinguish the central potential $V_c(r)$ (first term) and the spin-orbit interaction potential $V_{s-o}(r)$ (second term) where $\vec{L} \cdot \vec{\sigma}$ depends on j, l and s:

$$\vec{L} \cdot \vec{\sigma} = j \cdot (j+1) - s \cdot (s+1) - l \cdot (l+1) \tag{77}$$

A graphic representation example of this total potential $V_T(r)$ and its different components in the proton case, for the particular partial wave $p_{1/2}$ and energy $E_p = 6\,MeV$ is shown on Figure 2 by the continuous lines. Also, represented points are the values that each small square well is going to take as its potential depth.

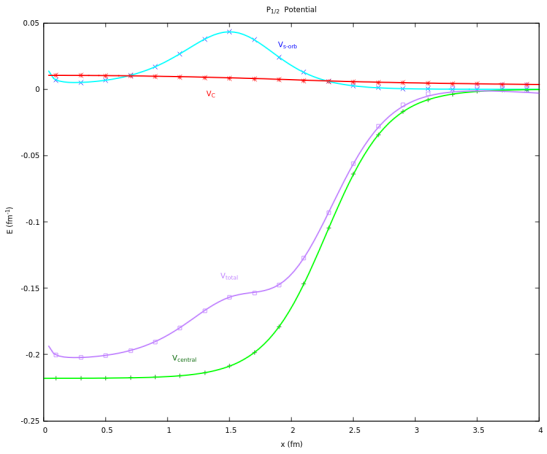

Figure 2: Total proton potential example for $p_{1/2}$ partial wave and their constituent parts at a fixed energy $E_p = 6MeV$. Lines represent analytic functions and points are the evaluated values of potential at the N_{sw} that are going to be used for the graining.

In equation (76):

$$\begin{aligned} x &= (r-R)/a, \qquad & x_s &= (r-R_s)/a_s \\ R &= r_0(M_\alpha/M_p)^{\frac{1}{3}} \qquad & R_s &= r_s(M_\alpha/M_p)^{\frac{1}{3}} \end{aligned} \tag{78}$$

Where $M_\alpha/M_p = 3.973$ value is taken. For the proton Coulomb potential we use a charge radius $R_C = 1.3(M_\alpha/M_p)^{\frac{1}{3}}$. In "An Optical model for the scattering of nucleons from ^4He at energies below 20 MeV" [7], after some calculations and optimizations, potential parameters are chosen as:

$$\begin{aligned} V_n &= 41.8MeV, \qquad & V_{sn} &= (3.0+0.1E_n)MeV \\ V_p &= 43.0MeV, \qquad & V_{sp} &= (2.7+0.1E_p)MeV \\ r_0 &= (1.50-0.01E)fm, \qquad & r_s &= 1.0fm \\ a &= a_s = 0.25fm \end{aligned} \tag{79}$$

In order to solve the Schrödinger equation using the square potential graining we set a reasonable number of square wells $N_{sw} = 20$, what means that increasing the number of them does not improve results significantly any longer. This approximation is done by splitting the potential into N_{sw} square wells centered in equally-spaced points going from $r = 0$ to $r = a_N$ with the same width, $w_n = \frac{a_N}{N_{sw}}$, each of them with a different potential value determined by evaluating the total potential $V_T(r)$ expression, Equation (76) in the center of each well. In Figure 3 we can actually see how this potential graining is done taking each $V_{Ti}(r)$ value as the one evaluated in the center of the considered square well.

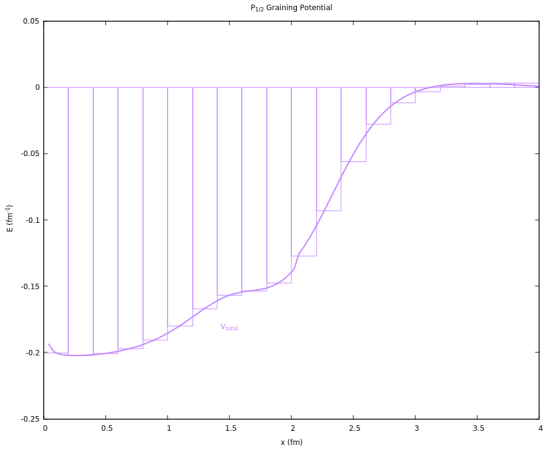

Figure 3: Total potential graining example for $p_{1/2}$ partial wave.

8 Optical model main results reproduced using the graining potential approximation.

The reaction that we are going to study is scattering of α particle with protons and neutrons. It is a particular case in which the incident particles have spin $\frac{1}{2}$ and the target particle ^4He is spinless. We make a first calculation using previous section grained potential for a range of energies between 0 to 20 MeV for which inelastic processes are not of important relevance. Potential range R_{max} is approximated to be $a_N = 4fm$.
We will assume that the potential is negligible (~ 0) at $r > a_N$ in the neutron case and there exist a Coulomb potential V_C at $r > a_N$ in the proton one. As we explained in Section 3.2, the expansion of the wave function in terms of partial waves does not contain infinite number of them contributing to the scattering amplitude. There is a maximum value of partial waves l_{max} that are actually influenced by the interaction ($l \leq l_{max} \sim ka_N$). In our study l_{max} for both neutron and proton (as their mass difference is not relevant) can be approximated:

$$l_{max} = \sqrt{2\mu E_{max}} R_{max} = 3.51 \approx 4 \tag{80}$$

This means we are going to consider waves up to $l < 4$ (s,p,d,f)

8.1 Phase Shifts Calculation

The first calculation and most important one consists on determining phase shifts of these partial waves at different energies from 0 to 20 MeV. Using the square-well method, we are able to calculate those values numerically. Some representative values have been obtained. The ones providing the most important partial waves contributions (s,p) are given in Table 1 and represented in Figure 4.

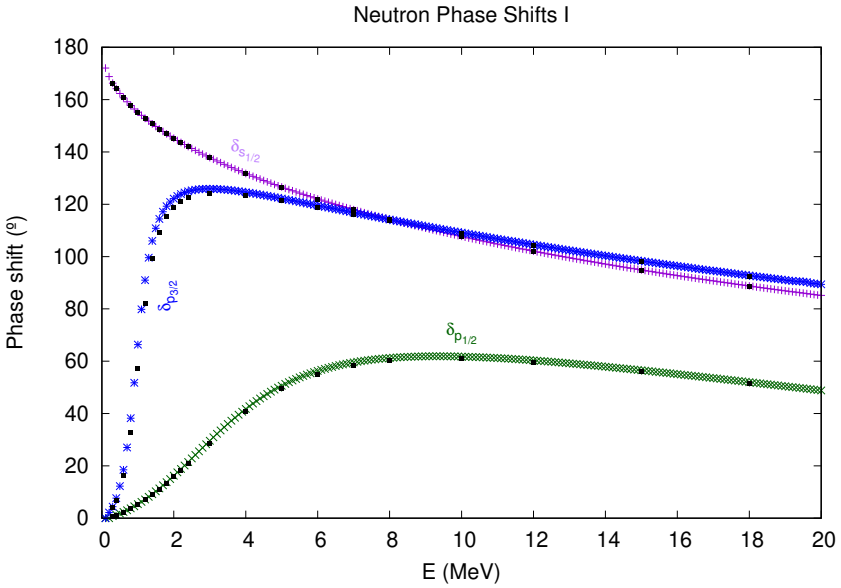

Figure 4: Neutron Phase Shifts $\delta(^o)$ obtained for $s_{1/2}$, $p_{1/2}$ and $p_{3/2}$ partial waves for an energy range 0 to $20MeV$ using the square wells method. Black points are the same result obtained by G.R.Satchler and L.W.Owen [7] using the optical continuous potential.

$E_{\mathrm{nn}}(MeV)$	$\delta_0^{1/2}$	$\delta_1^{1/2}$	$\delta_1^{3/2}$
0.2	168.80	0.44	2.16
0.4	164.19	1.27	7.68
0.6	160.68	2.39	18.51
1.0	155.16	5.36	66.33
1.5	149.73	10.27	110.80
2.0	145.22	16.23	122.14
2.5	141.310	22.85	125.30
3.0	137.82	29.610	125.910
3.5	134.67	36.03	125.50
4.0	131.77	41.77	124.59
4.5	129.09	46.64	123.45
5.0	126.58	50.63	122.18
5.5	124.23	53.81	120.85
6.0	122.02	56.28	119.50
7.0	117.94	59.56	116.79
8	114.23	61.24	114.15
11.0	104.80	61.20	106.79
14.0	97.15	57.91	100.30
17.0	90.70	53.54	94.54
20.0	85.15	48.84	89.38

Table 1: Neutron Phase Shifts $\delta(^{\mathrm{o}})$ of $s_{1/2}$, $p_{1/2}$ and $p_{3/2}$ partial waves calculated using square wells. E_n corresponds to the energy of the incident neutron in the laboratory frame.

In Figure 4 we can see the phase shifts of $l = 0$ and $l = 1$, that are the main contribution to the partial wave expansion at this energy range. Some known characteristics of these phase shifts can be seen in our results: In $p_{3/2}$ phase shift we find a very quick change of its value around $E = 1MeV$. This is a sign that there is a resonance in the interaction, which corresponds to the known ^5He state. Also in the proton case (Figure 6) a resonance is observed, this one correspond to the ^5Li state. In both cases the nuclear shell model predicts the filling process to start at $p_{3/2}$, just where the resonance is observed. Another standing up result is the $s_{1/2}$ phase shift value at low energies. The non-relativistic quantum scattering Levinson theorem states:

$$\delta_l(0) - \delta_l(\infty) = n_b\pi \tag{81}$$

This theorem relates the number of potential bound states n_b with the difference in phase of a scattered wave at zero and infinite energy. In our case it predicts a non-existing bound state as the extracted value of $\delta_l(0)$ from Figure 4 is $\delta_l(0) = 180^{\mathrm{o}} = \pi$ but neither $p - {}^4He$, $n - {}^4He$ systems have any bound state. That is because they are forbidden by the Pauli Principle at the level of nucleons as discussed in "Refinement of the $n-\alpha$ fish-bone potential" [8]. We can affirm this result is a spurious bound state.

As we may see, the result obtained in our approximation is very similar to the one obtained using a continuous potential function obtained by G.R.Satchler and L.W.Owen [7] and their different way of solving the Schrödinger equation.

We obtain smaller phase-shifts values for $l = 2$ and $l = 3$ but they are still not negligible in our calculations. Some of the values are given in Table 2 and the phase shifts representation is shown in Figure 5

$E_{\mathrm{nn}}(MeV)$	$\delta_2^{3/2}$	$\delta_2^{5/2}$	$\delta_3^{5/2}$	$\delta_3^{7/2}$
2.0	0.05	0.07	0.00	0.00
3.0	0.13	0.18	0.00	0.00
4.0	0.25	0.35	0.00	0.00
5.0	0.41	0.59	0.01	0.01
6.0	0.60	0.88	0.01	0.02
7.0	0.81	1.23	0.02	0.03
8.0	1.05	1.64	0.03	0.04
9.0	1.30	2.09	0.04	0.05
10.0	1.56	2.59	0.05	0.07
11.0	1.82	3.13	0.07	0.10
12.0	2.08	3.71	0.08	0.12
13.0	2.34	4.31	0.10	0.15
14.0	2.58	4.94	0.12	0.19
15.0	2.81	5.59	0.13	0.23
16.0	3.02	6.25	0.15	0.27
17.0	3.21	6.92	0.17	0.31
18.0	3.37	7.59	0.19	0.36
19.0	3.51	8.27	0.21	0.41
20.0	3.62	8.94	0.22	0.47

Table 2: Neutron Phase Shifts $\delta(^{\circ})$ of $d_{3/2}$, $d_{5/2}$, $f_{5/2}$ and $f_{7/2}$ partial waves calculated using square wells. E_{nn} corresponds to the energy of Neutron in the laboratory frame.

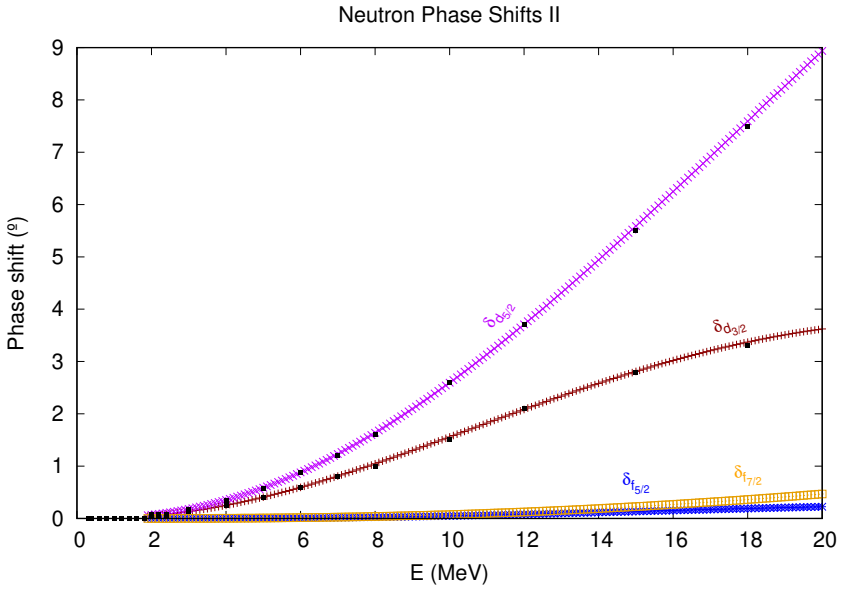

Figure 5: Neutron Phase Shifts $\delta(^{\circ})$ obtained for $d_{3/2}$, $d_{5/2}$, $f_{5/2}$ and $f_{7/2}$ partial waves for an energy range 0 to $20MeV$ using the square wells method. Black points are the same result obtained by G.R.Satchler and L.W.Owen [7] using the optical continuous potential.

As expected, much smaller values of phase shifts are obtained for $l = 2$ and $l = 3$.We found them to be smaller by orders of magnitude. Contributions to the relevant scattering parameters are going to be considerably smaller than those of the $l = 0$ and $l = 1$ partial waves at these concrete energy ranges. Nevertheless, they are still important in partial wave expansion.

Analogously, using Coulomb functions at $r > a_N$ instead of spherical Bessel ones we obtain very similar results for the proton scattering. This is reasonable since Coulomb potential V_C contribution inside the potential range is considerably small as can be easily seen in Table 3.

$E_{\mathrm{pp}}(MeV)$	$\delta_0^{1/2}$	$\delta_1^{1/2}$	$\delta_1^{3/2}$
1.0	167.82	1.92	7.10
1.5	162.11	4.48	22.06
2.0	157.23	8.03	51.67
2.5	152.95	12.45	83.60
3.0	149.12	17.58	101.61
3.5	145.64	23.14	110.06
4.0	142.45	28.83	114.07
4.5	139.50	34.33	115.93
5.0	136.75	39.38	116.64
5.5	134.17	43.82	116.70
6.0	131.75	47.61	116.37
6.5	129.46	50.75	115.78
7.0	127.28	53.30	115.03
8.0	123.24	56.90	113.24
10.0	116.15	59.99	109.22
12.0	110.06	60.00	105.14
14.0	104.73	58.47	101.20
16.0	99.99	56.17	97.47
18.0	95.72	53.45	93.94
20.0	91.84	50.53	90.62

Table 3: Proton Phase Shifts $\delta(^{\mathrm{o}})$ of $s_{1/2}$, $p_{1/2}$ and $p_{3/2}$ partial waves calculated using square wells. E_{pp} corresponds to the energy of the proton in the laboratory frame.

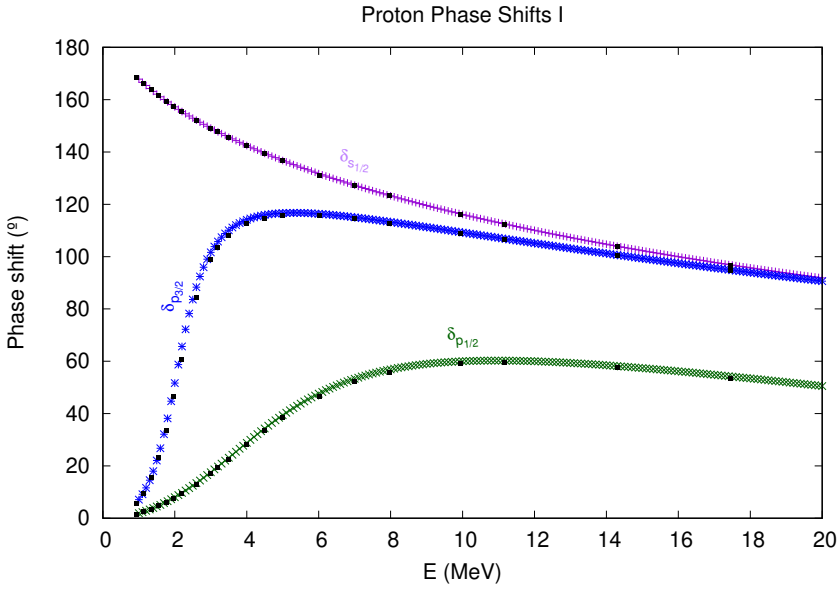

Figure 6: Proton Phase Shifts $\delta(^{\circ})$ obtained for $s_{1/2}$, $p_{1/2}$ and $p_{3/2}$ partial waves for an energy range 0 to $20MeV$ using the square wells method. Black points are the available results obtained using a continuous potential (optical approximation)[7].

$E_{\rm pp}(MeV)$	$\delta_2^{3/2}$	$\delta_2^{5/2}$	$\delta_3^{5/2}$	$\delta_3^{7/2}$
2.0	0.03	0.04	0.00	0.00
3.0	0.08	0.11	0.00	0.00
4.0	0.18	0.24	0.00	0.00
5.0	0.30	0.41	0.01	0.01
6.0	0.46	0.64	0.01	0.01
7.0	0.64	0.93	0.02	0.02
8.0	0.85	1.26	0.02	0.03
9.0	1.08	1.65	0.03	0.04
10.0	1.33	2.08	0.04	0.06
11.0	1.58	2.54	0.06	0.08
12.0	1.83	3.05	0.07	0.10
13.0	2.09	3.58	0.09	0.13
14.0	2.33	4.14	0.11	0.16
15.0	2.57	4.73	0.12	0.19
16.0	2.79	5.33	0.14	0.23
17.0	3.00	5.94	0.16	0.27
18.0	3.18	6.56	0.18	0.32
19.0	3.35	7.18	0.20	0.36
20.0	3.48	7.82	0.22	0.41

Table 4: Proton Phase Shifts $\delta(^{\circ})$ of $d_{3/2}$, $d_{5/2}$, $f_{5/2}$ and $f_{7/2}$ partial waves calculated using square wells. E_{pp} corresponds to the energy of the proton in the laboratory frame.

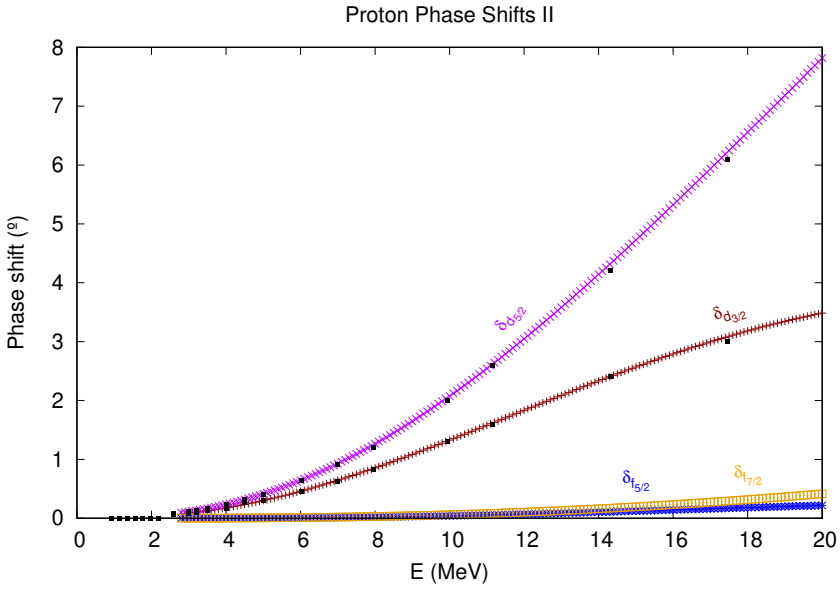

Figure 7: Proton Phase Shifts obtained for $d_{3/2}$, $d_{5/2}$, $f_{5/2}$ and $f_{7/2}$ partial waves for an energy range 0 to $20MeV$ using the square wells method. Black points are available results obtained using a continuous potential (optical approximation) [7].

8.2 Differential cross Section calculation

Once we have determined the phase shifts, we are able to calculate the most important observables. Differential cross section can be determined for a chosen energy. As an example, differential cross sections and polarizations at energies between 2 and 16 MeV were calculated. These results have been compared both to the ones calculated by the optical approximation [7] and the experimental obtained values by B.Hoop in "Scattering of neutrons by α particles [9] and T.H May, "Scattering of Polarized Neutrons by α particles [11]. Results for the neutron and proton scattering are plotted in Figure 8 (Differential cross section) and Figure 9 (polarization). In order to make differences in energies more visual, since plots are very similar, we have multiplied differential cross section by 10 when decreasing energy to have a well-separated curve for each energy case in the same graph. In polarization results, polarization values are shifted an unit from one to other for the same reason.

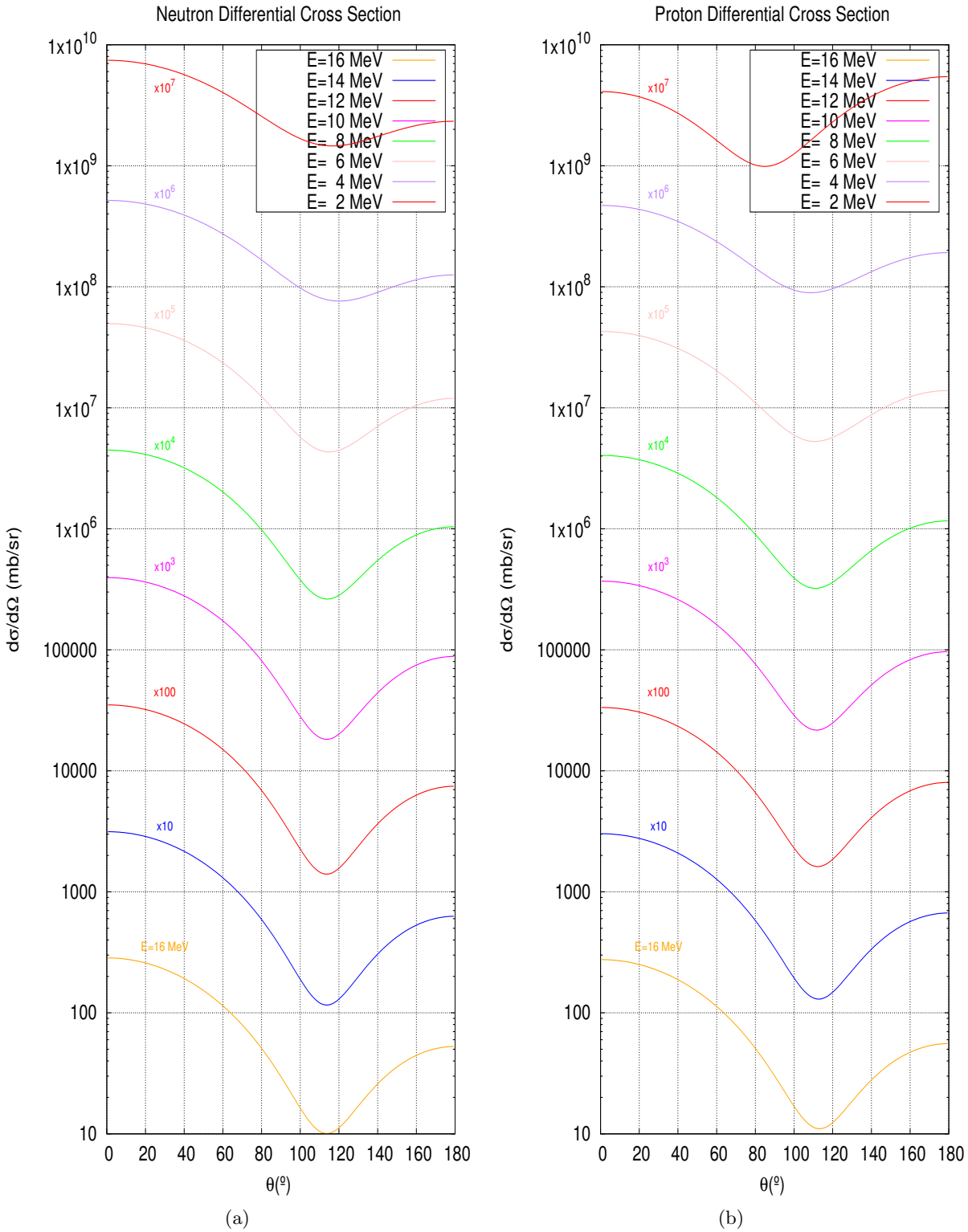

(a) (b)

Figure 8: Differential cross sections calculated for some energies. E is the energy of the incident particle in the LAB frame. (a) Neutron Differential Cross Section; (b) Proton Differential Cross Section.

Analogously, we calculate neutron and proton polarizations.

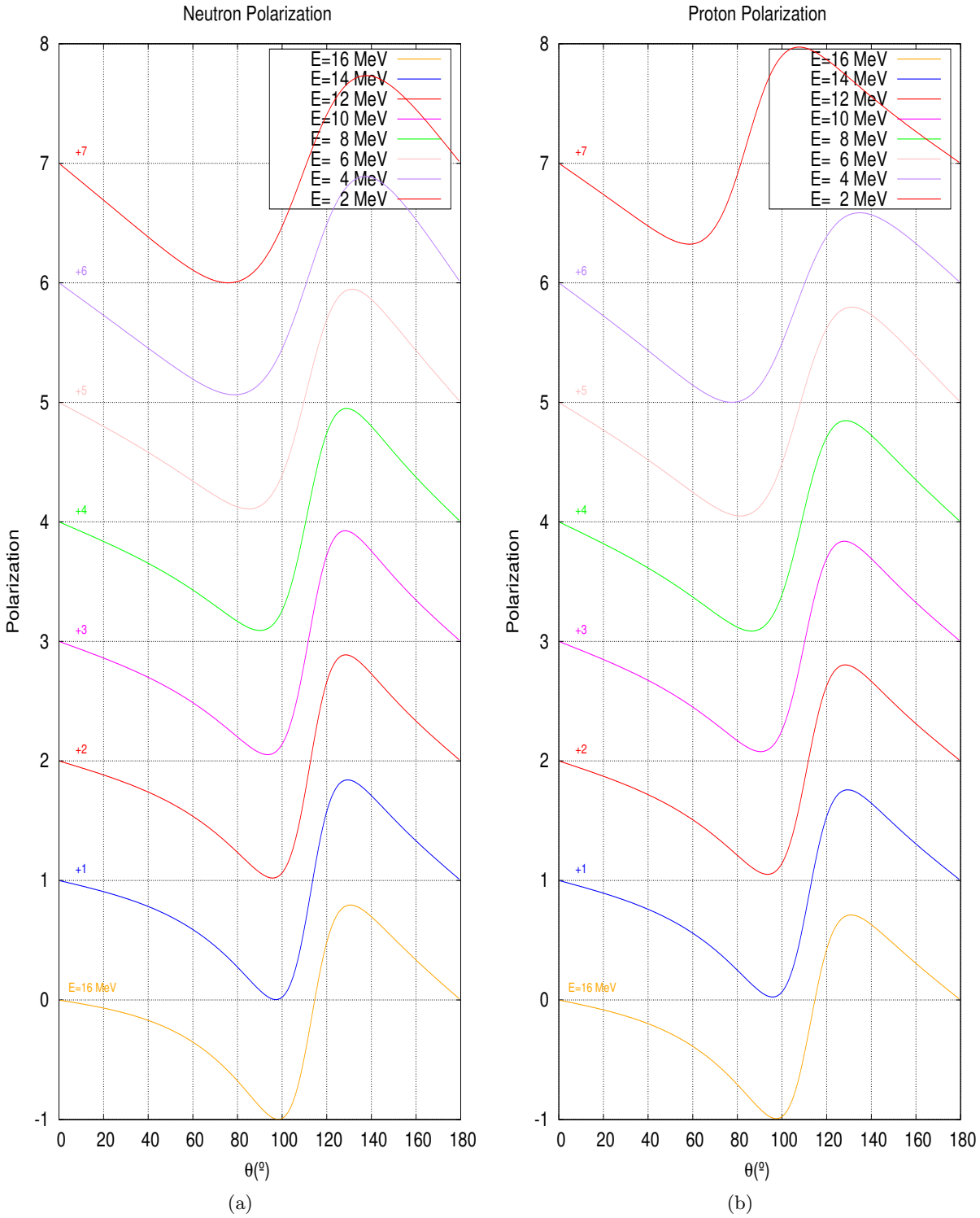

Figure 9: Polarization calculated for some energies. E is the energy of the incident particle in the LAB frame. (a) Neutron Polarization; (b) Proton Polarization.

9 Potential graining parameters

We have reproduced the most important previous results obtained by G.R.Satchler and L.W.Owen [7] using our square-well approximation and non-appreciable differences respect to the Optical Approximation have been appreciated. At this point we may rely on the graining method and leave aside the Optical Potential used to assign values to our parameters. We instead aim to make a suitable fit to the experimental data in order to obtain their values. Those fitting parameters are the depth energy values of each square well composing the grained potential.
The most important idea under our solution method is that it is not efficient or, in any case, necessary to introduce more parameters than experimental resolution can probe, as discussed in "Partial wave analysis of Chiral NN interactions" [12]. Because of the uncertainty principle $\Delta r \Delta p \geq \frac{\hbar}{2}$:

$$\Delta r \sim \frac{1}{p_{max}} \tag{82}$$

The potential graining we are doing relates width, number of square wells and potential range as follows:

$$\Delta r N_{sw} = a_N \tag{83}$$

By replacing equation (82) into (83) we get an equation that directly relates number of square wells and energy of the incident particle:

$$N_{sw} = a_N \sqrt{2\mu E} \tag{84}$$

Where we have used $p_{max} = p_{CM} = \sqrt{2\mu E_{CM}}$
It should be possible to reproduce the experimental data and get information about the potential using just $2N_{sw}$ parameters. The potential description is done adding up $(V_c + V_C)$ as a whole and then the spin-orbit term V_{s-o} multiplied by $\vec{\sigma}\vec{L}$, whose value depends on j and l values for each partial wave (See eq (77)). Then:

$$V_{T(i)}(r) = V_i(r) + \vec{\sigma}\vec{L} \cdot V_{s-o(i)}(r) \qquad\qquad i = 1, 2...N_{sw} \tag{85}$$

The idea is to minimize the difference between the experimental data and the obtained value using this potential function. Then we may get those N_{sw} parameters using statistics distribution theory. In our case we consider a limiting maximum energy of $23.8MeV$ then :

$$N_{sw} = a_N \sqrt{2\mu E} = 3.83 \ \sim 4 \tag{86}$$

We can make the approximation of the potential as a sum of V_n, and V_{ns} $(n = 1...4)$ square wells, a total of 8 parameters.

9.1 Fitting process

The fitting process is done by minimizing the χ^2 distribution, directly comparing the theoretical result obtained with the grained potential method and the experiment values as discussed in [16]. The χ^2 expression and characteristics are studied in "The Chi-Squared test for a distribution" J.R. Taylor [5].

$$\chi^2 = \sum_{1}^{N_{dat}} \frac{(x_{sw} - x_{exp})^2}{(\Delta_{exp})^2} \tag{87}$$

Where x_{sw} represents either a differential cross section value obtained by the square-well method or a polarization one, depending on the case. x_{exp} is the same experimental observable value and Δ_{exp} is the associated experimental error.

9.2 Experimental data set.

Experimental data has been taken from the Experimental Nuclear Reaction Data (EXFOR) database. We are going to work with one of the two reactions ($n - {}^4He$). Differential cross section and polarization data of neutrons in the range 0-22 MeV were selected from different scattering experiments. A total of 202 data are taken into account in the χ^2 minimization process where 98 of them are differential cross section data and 104 are polarization measurements. The energies and covered scattering angles of the data set can be summarized in Table 5.

$E(MeV)$	$\theta_{range}(^o)$	N_{data}
17.72	31.2-149.4	14
14.1	63.3-161.8	15
14.3	25-85	7
16.4	64-149.5	62

(a)

$E(MeV)$	θ_{range}	N_{data}
3.38	73-149.3	7
7.8	49.6-149.35	9
11	47.7-159.1	17
17.7	47.7-159.1	12
23.8	47.7-159.1	13
17	47.8-153.7	11
14	46.8-152.5	11
15	61.4-165.7	12
17	61.4-165.7	12

(b)

Table 5: Experimental $n - {}^4He$ scattering data. E is the energy of the incident particle in the LAB frame and θ is the scattering angle measured in the CM frame. (a) Differential cross section data , (b) Polarization Data

.

9.3 Minimization process using Downhill Simplex Method.

This multidimensional method consists of building a geometrical figure (Simplex) of N+1 vertices in an N-dimensional space (where N is the number of parameters to be fitted). The Simplex is built enclosing the searched minimum. Then the function is evaluated in each vertex and the results are compared. The vertex with the largest obtained value of the function (in our case χ^2) is modified by reflection, contraction or expansion depending on the case. The process is repeated until a pre-selected tolerance (difference between all evaluated vertices) is reached. In order to start a multidimensional minimization, we might give our algorithm a starting guess. Building a N+1 simplex requires a $N \times (N+1)$ starting matrix where the rows contain N-vectors of the independent variables and columns different initial values of the same variable. In our particular case, a $2N_{sw} \times (2N_{sw}+1)$ matrix is needed to build up the simplex. The values in the columns of the initial matrix have been carefully taken closed to the expected minimum (comparing it with the optical model) and taking into account the χ^2 dependence on each parameter. If weak dependence of χ^2 on an individual parameter value was found then a largest range of possible values was selected. On the other hand, if strong χ^2 dependence is observed then the range of values of the initial parameter is defined narrower. (See Figure 10).

V_n	$E_{range}(MeV)$	$V_{n\,s-o}$	$E_{range}(MeV)$
V_1	-48,-39	V_{1s}	-5,-0.5
V_2	-44,-30	V_{2s}	-10,-2.5
V_3	-10,-1.9	V_{3s}	-5,-0.2
V_4	-4,-1.5	V_{4s}	-3,-0.1

Table 6: Range of V_n and V_{ns} selected for the initial simplex.

V_n	$E_{range}(MeV)$	$V_{n\,s-o}$	$E_{range}(MeV)$
V_1	-51.55	V_{1s}	-4.54
V_2	-39.92	V_{2s}	-6.68
V_3	-11.99	V_{3s}	-0.59
V_4	1.37	V_{4s}	-0.59

Table 7: Parameter Values obtained after downhill Simplex Method minimization

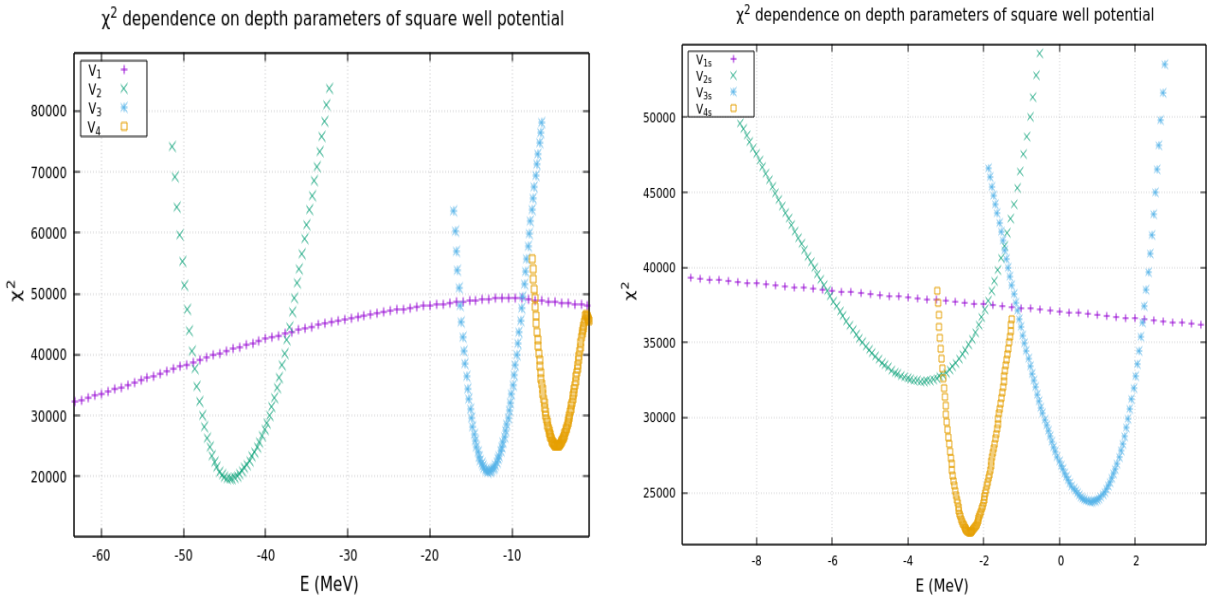

(a) (b)

Figure 10: χ^2 dependence on the individual parameters. (a)Central Potential part. (b)Spin-orbit Potential part.

After the minimization process, we obtain the results shown in Table 7. These calculated potential values and the optical approximation model ones are shown in Figure 11.

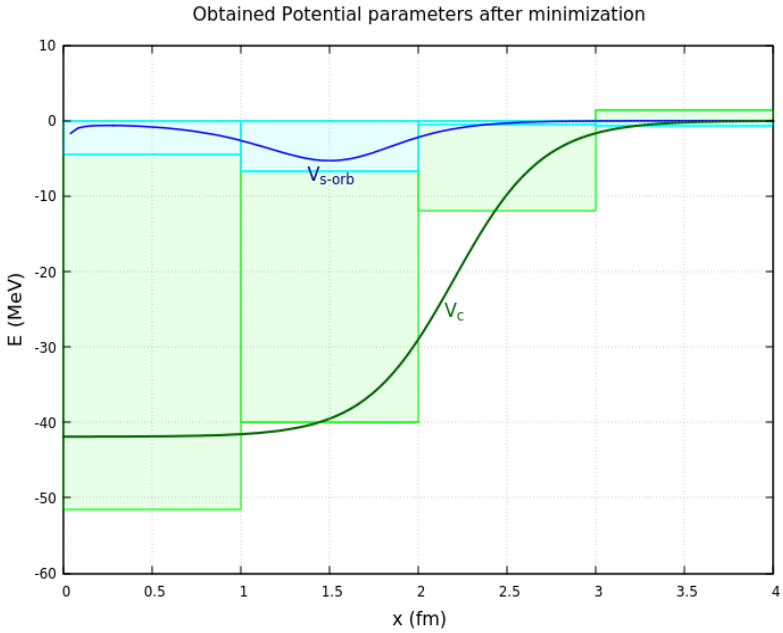

Figure 11: Neutron Optical Potential ($E = 11 MeV$) and its grained square well potential approximation using the minimum values after the minimization process.

9.4 Weight of different parameters to the fit.

When analyzing the χ^2 dependence on the different parameters we found some of them were considerably more important than others in the fitting process.(See Figures 10a and 10b) We had the hypothesis that this fact was directly related to the impact parameter b of the incident particle. Each given experiment with an energy value E and a scattering angle θ has an associated classical impact parameter b. Depending on this parameter, we can see details of the potential up to a certain range. The smallest the impact parameter, the innest part of the potential we can explore. The deflection function, Equation (88) is used in order to relate those variables (E, θ, b) :

$$d\theta = \int_{r_{min}}^{\infty} \frac{-b}{r^2 \sqrt{1 - \frac{V(r)}{E} - \frac{b^2}{r^2}}} dr \tag{88}$$

This classical function is an approximation where the time dependence has been removed, thus no resonance effects could be taken into account as, for example, the particular case shown in Figure 12.

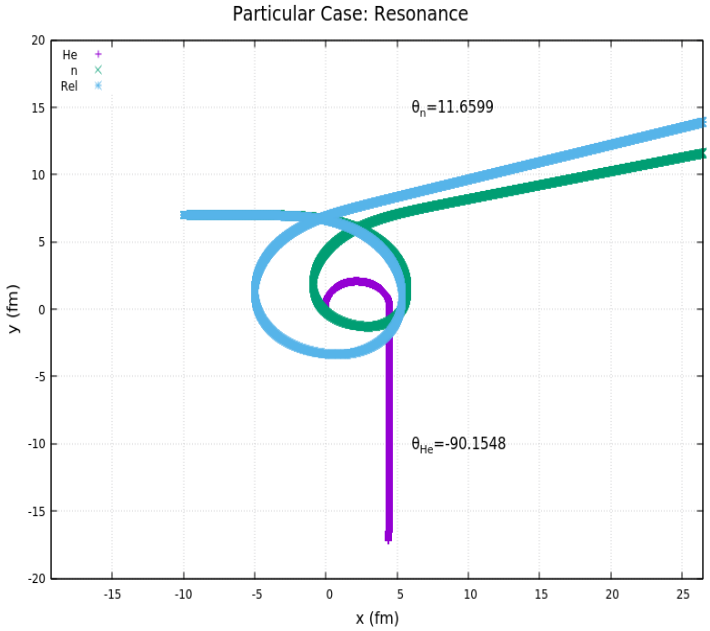

Figure 12: Classical Resonance Example: Obtained for a Wood-Saxon Potential $V_0 = -10\,MeV$, $a = 0.8\,fm$ where the incident particle has energy $E = 2.5\,MeV$ and an impact parameter $b = 7fm$. Purple line represent the target trajectory, the green one the projectile trajectory and the blue one corresponds to the relative trajectory.

To obtain a time-dependent solution of these variables, we solve directly the classical equations of motion eq (89). In the non-relativistic case numerically. We approximate the potential to a Wood-Saxon form, Equation (90) with the concrete parameter values $R = 2.5\,fm$, $a = 0.2$ and $V_0 = -40\,MeV$

$$m\frac{d^2x}{dt^2} = -\left(\vec{\nabla}V\right)_x \quad , \quad m\frac{d^2y}{dt^2} = -\left(\vec{\nabla}V\right)_y \tag{89}$$

$$V(r) = \frac{V_0}{1 + e^{\frac{r-R}{a}}} \tag{90}$$

This system of differential equations has been solved using the Euler method where we calculate by iteration from some initial values of the particles using the first order approximation:

$$\begin{pmatrix} x(t+h) \\ v_x(t+h) \end{pmatrix} = \begin{pmatrix} x(t) \\ v_x(t) \end{pmatrix} + h \begin{pmatrix} v_x(t) \\ a_x(t) \end{pmatrix} \tag{91}$$

$$\begin{pmatrix} y(t+h) \\ v_y(t+h) \end{pmatrix} = \begin{pmatrix} y(t) \\ v_y(t) \end{pmatrix} + h \begin{pmatrix} v_y(t) \\ a_y(t) \end{pmatrix} \tag{92}$$

We can reproduce the trajectory of the particles and the relative trajectory as well for a given incident energy E and impact parameter b (See Figure 13).

From them we can obtain the associated scattering angle.

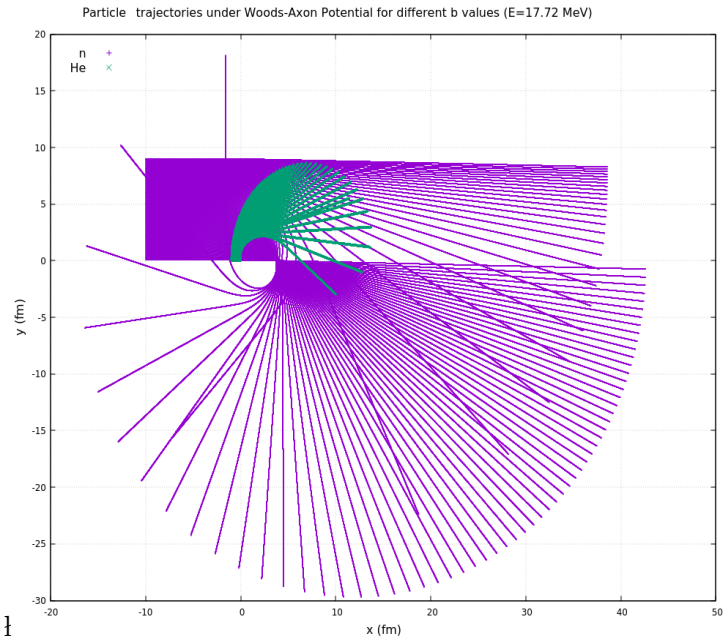

Figure 13: Example of obtained trajectories for different impact parameter b used to calculate scattering angles $E = 17.72\,MeV$ and an impact parameters from $b = 0fm$ to $b = 9fm$. Purple lines represent the incident particle while green ones are the target trajectories.

Once we have a table with enough different impact parameter trajectories we can associate a b value to each one of our concrete experimental energies E and scattering angles θ. The result of impact parameters obtained in a distribution form is shown in Figure 14.

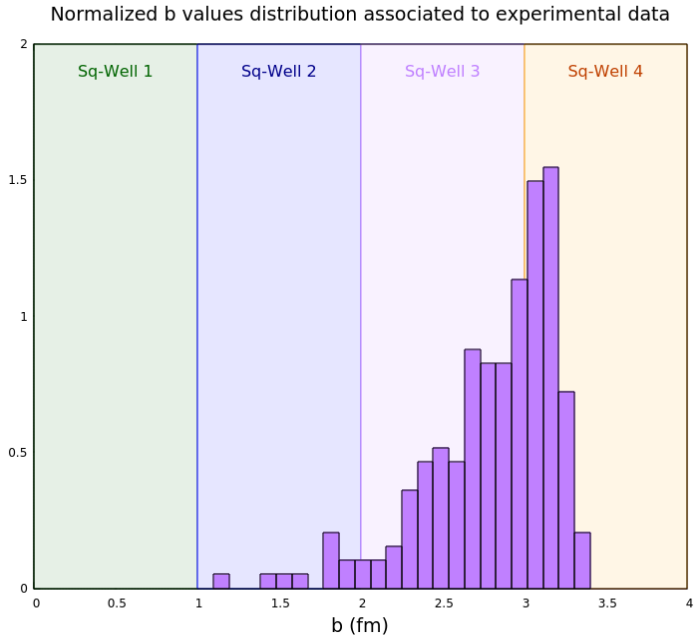

Figure 14: Impact parameter values distribution associated to our experimental set.

Although this calculation is a classical approximation of our concrete case and also a Wood-

Saxon potential has been taken, the fact that none of the experimental data is associated to an impact parameter lower than $1fm$ can explain why the potential depths of the first square wells have the weakest influence when minimizing the χ^2, while the other square well parameters have a stronger one, especially the central ones.

10 Monte Carlo Simulation-Bootstrap method.

.

As suggested in [17], an alternative strategy for propagating errors of nuclear forces in nuclear structure calculations can be done using a Monte Carlo bootstrap. Instead of using the obtained minima and aiming to estimate the minimization errors, we suppose that each one of the experimental data used in the fit is composed by N independent and gaussian distributed values around it with $\sigma = \Delta_{exp}$, where Δ_{exp} is the error of each particular datum. (See an example data distribution in Figure 15). We generate a total of N events for each experimental datum. With each one of these different "experimental" input values, the calculated observables (differential cross sections and polarizations) and the obtained minimization parameters become distributions, e.g, we obtain N different set of parameters that minimize the χ^2 function in each case. Once we have the distributions it is possible to take the mean values and calculate the 68% confidence intervals that are going to determine our error estimation bands.

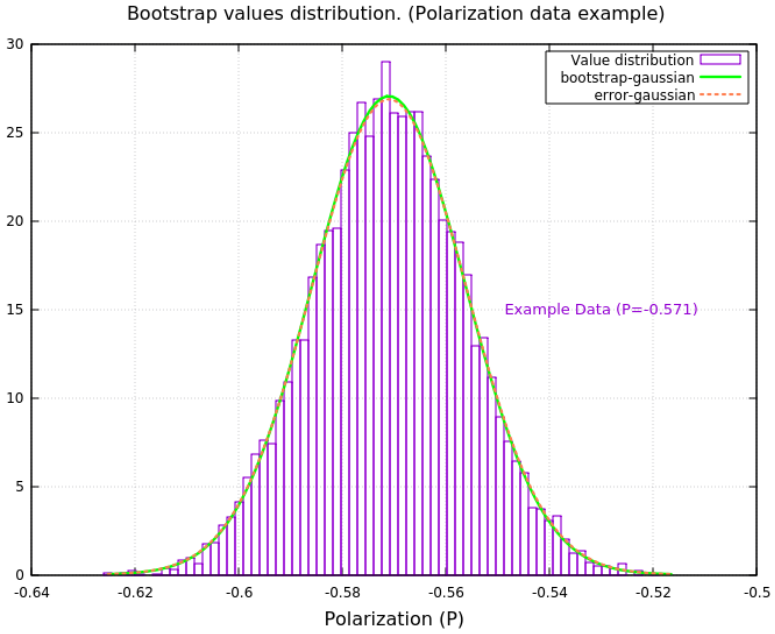

Figure 15: Gaussian distributed values generated for an experimental data point in the Bootstrap method. Example of polarization data measured for incident energy $E = 17\,MeV$ and scattered angle $\theta = 104.8^{o}$. The obtained gaussian after the Bootstrap method (green line) together with the error estimation one (dashed orange one) are also represented.

All data points were generated as explained before a total of 10000 times in a gaussian distribution form, then using the downhill method the χ^2 function was minimized. 10000 different minimizing parameters sets and χ^2 values were obtained after the simulation. Representing the χ^2 dependence with each parameter (see Figure 16 and Figure 17), we observed how in some of the parameters, two different branches of solutions were being obtained. We also represent the obtained χ^2 distribution in Figure 18.

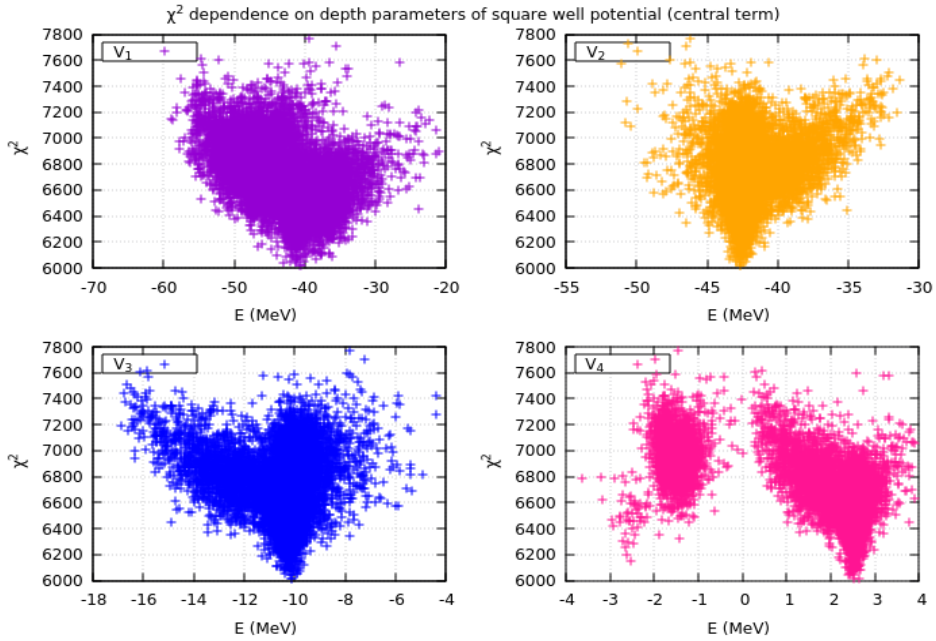

Figure 16: χ^2 distributions of each parameter of the central potential part obtained with the Bootstrap method. The Right-Bottom distribution of parameter V_4 shows two clearly distinguishable solution branches.

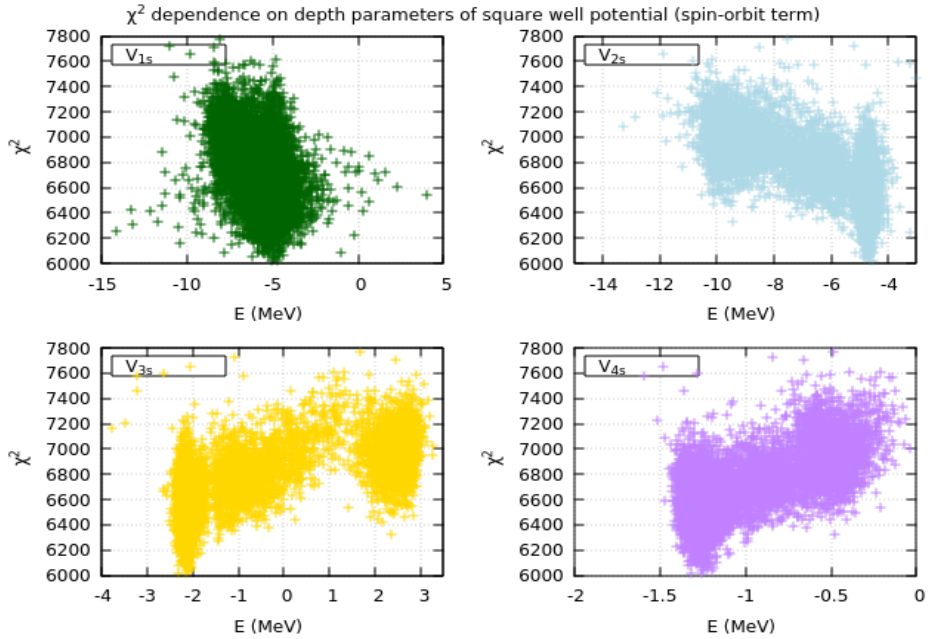

Figure 17: χ^2 distributions of each parameter of the spin-orbit potential part obtained with the Bootstrap method. Except the V_{1s} distribution, all parameters seem to have two solution branches.

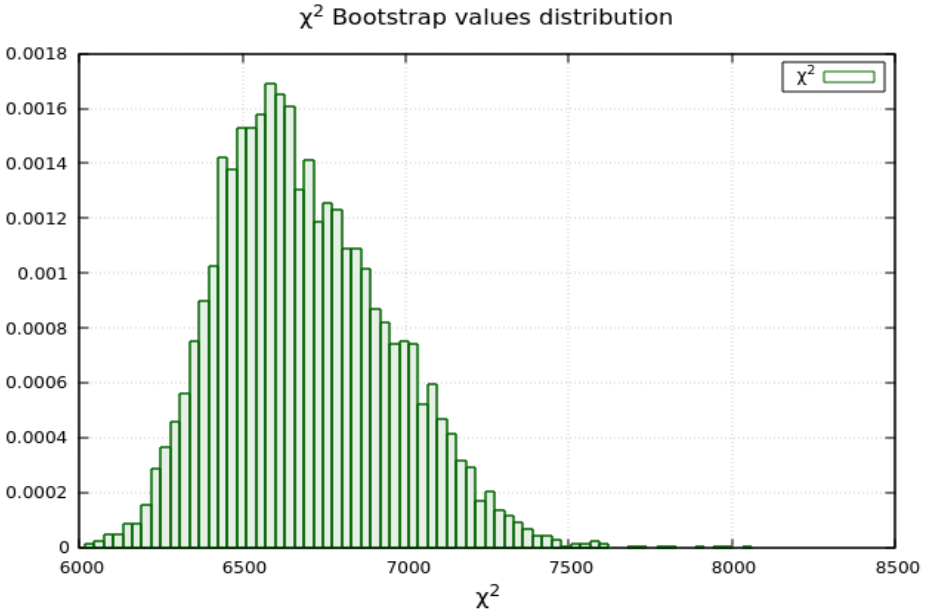

Figure 18: χ^2 distribution values obtained with the Bootstrap Method.

Fortunately, the obtained parameter values are not completely independent as we can see in the calculated correlation matrix in Figure 19, so we can study whether the independent-parameter branches obtained are part of a general set of parameters or not.

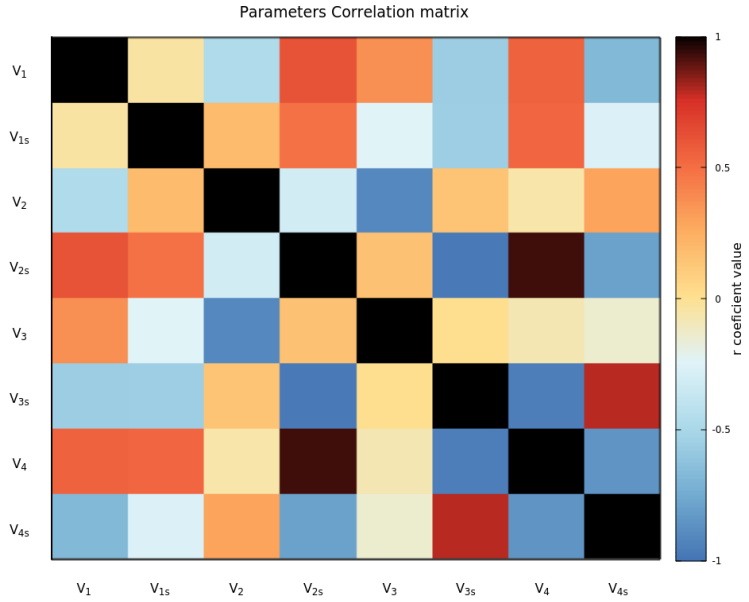

Figure 19: Parameter correlation matrix. Warm colors represent positive correlations while cold ones correspond to negative ones. Also, lighter ones infer low correlation and darker ones high correlation between parameters.

10.1 Selecting a solution branch.

If we represent the distributions in Figure 16 and 17 as histograms, we can observe the two solution branches that some of the parameter are taken. (See Figures 20 and 21)

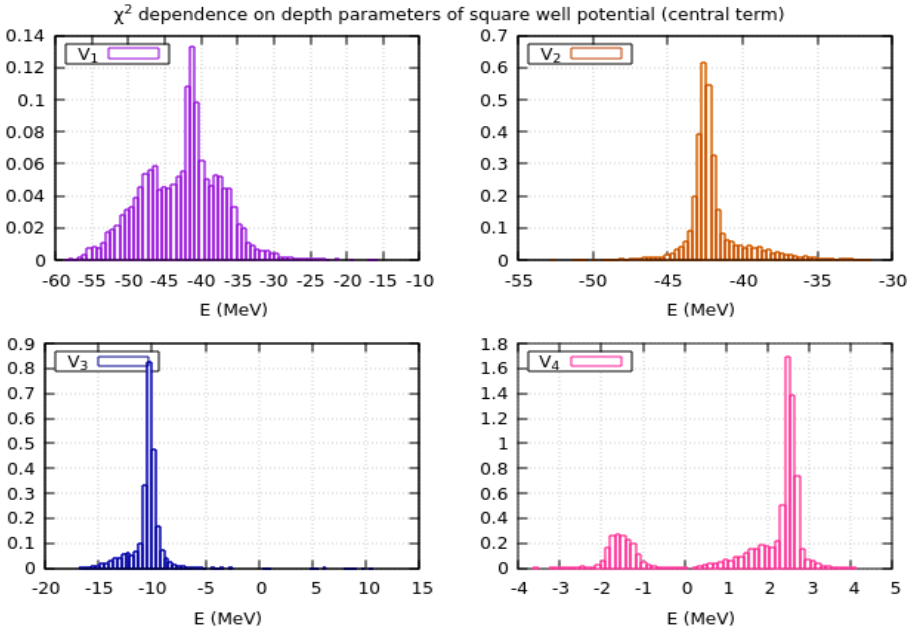

Figure 20: Histogram of the distributions values of each central potential parameter obtained with the Bootstrap method after minimizing the χ^2 function. In the V_4 parameter two branches are clearly distinguished.

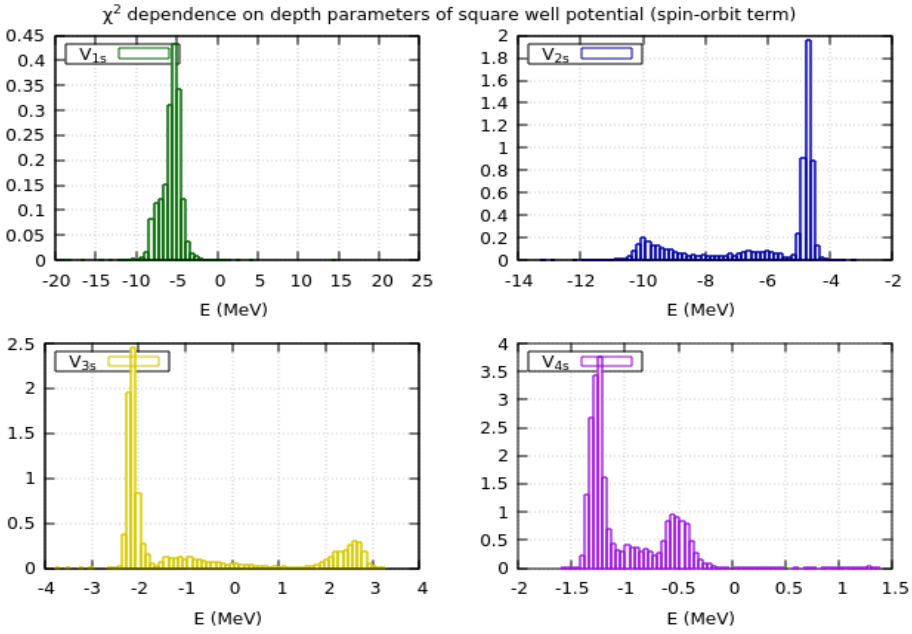

Figure 21: Histogram of the distributions values of each central potential parameter obtained with the Bootstrap method after minimizing the χ^2. Except for the V_{1s} parameter two solution branches are clearly distinguished.

We have first proved that each one of the individual parameter branches (most populated or less populated one) is correlated to the same (most populated or less populated) branch of a different parameter. (This effect can be seen in the correlation matrix in Figure 19, where the most correlated parameters are indeed the ones having the two different branches). We may see the solution as two different set of parameters branches.

Our criteria in order to select one of the solution branches has both a physical component and a statistical one. Suspecting that the model does not explain the low energy limit, where the interaction could have other effects that have not been taken into account as pion exchange, we excluded the only low energy data set containing a total of 7 experimental measurements and observed how the least populated branch decreased dramatically. A comparison of both distributions for the parameter V_{3s} is shown on Figure 22.

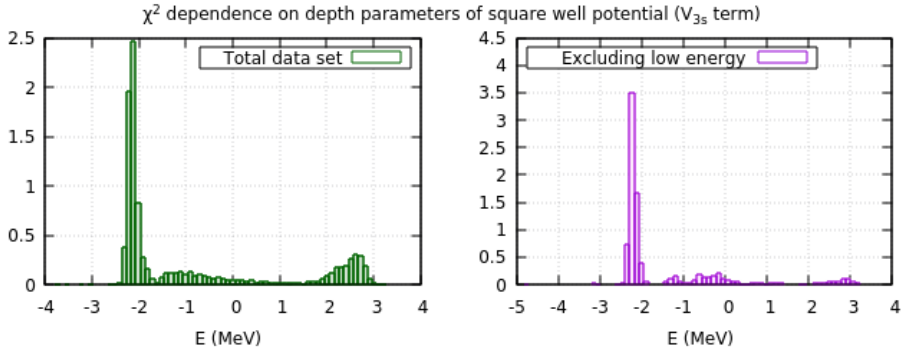

Figure 22: Histogram of the distributions values of the V_{3s} potential parameter obtained with the Bootstrap method after minimizing the χ^2 for the complete data set (left) and excluding low energy data (right).

Those parameters values unaffected after removing the low energy data corresponded in all cases to the branches containing considerably more events than the others. Both the statistical criteria and the physical one seem to be in accordance.

We decided to select a new initial simplex for the minimization process whose values were taken closely to the first obtained minimum and an unique solution branch was finally obtained.

10.2 Grained potential parameters results.

Once we have these distributions, we can obtain the values for each parameter that minimize the χ^2 function within that selected branch by taking the average value of their distributions. The associate error is taken as the 68% confidence limits and re-scaled in accordance with the χ^2 obtained value (see discussion in Section 10.5). The parameter values are shown in (Table 8 and represented in Figure 23).

V_n	$E_{range}(MeV)$	$V_{n\,s-o}$	$E_{range}(MeV)$
V_1	-41.6 ± 0.9	V_{1s}	-6 ± 2
V_2	-43.0 ± 0.3	V_{2s}	-4.6 ± 0.2
V_3	-9.9 ± 0.2	V_{3s}	-2.1 ± 0.1
V_4	2.46 ± 0.05	V_{4s}	-1.2 ± 0.1

Table 8: Parameter values obtained after Downhill Simplex minimization method and Bootstrap simulation. Associated errors are 68% confidence limits re-scaled in accordance with the χ^2 obtained value.

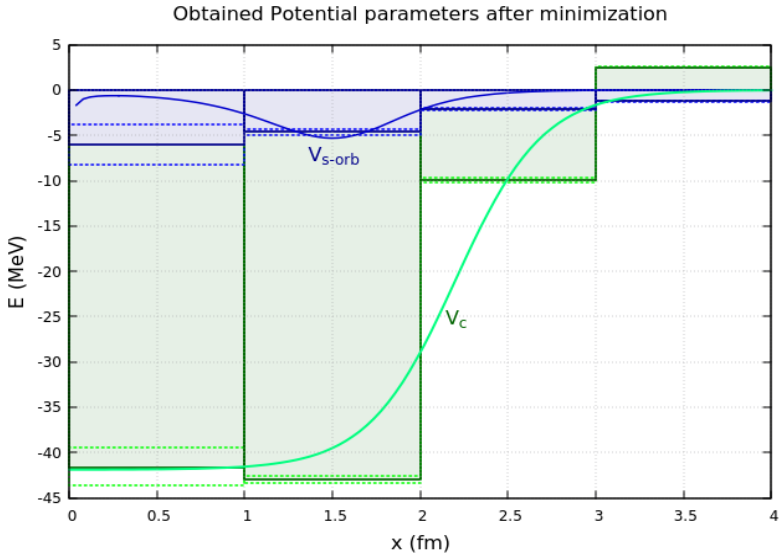

Figure 23: Optical Neutron Potential approximation (continuous lines), both central and spin-orbit contributions (green and blue lines respectively) are shown. Filled boxes values represent grained square well potential approximation using the average values after the minimization process using the Bootstrap method. Both central (green) and spin-orbit (blue) contributions to the total potential are shown. Dashed lines represent associated errors within 68% confidence limits after the selection of the branch. These errors are re-scaled in accordance with the χ^2 obtained value.

10.3 Differential Cross Section and Polarization results.

Using the selected branch we can get the average values of the different observables (differential cross sections and polarizations) and the 68% confidence limits of their distributions. The results are represented together with the experimental data in Figures 24 and 25.

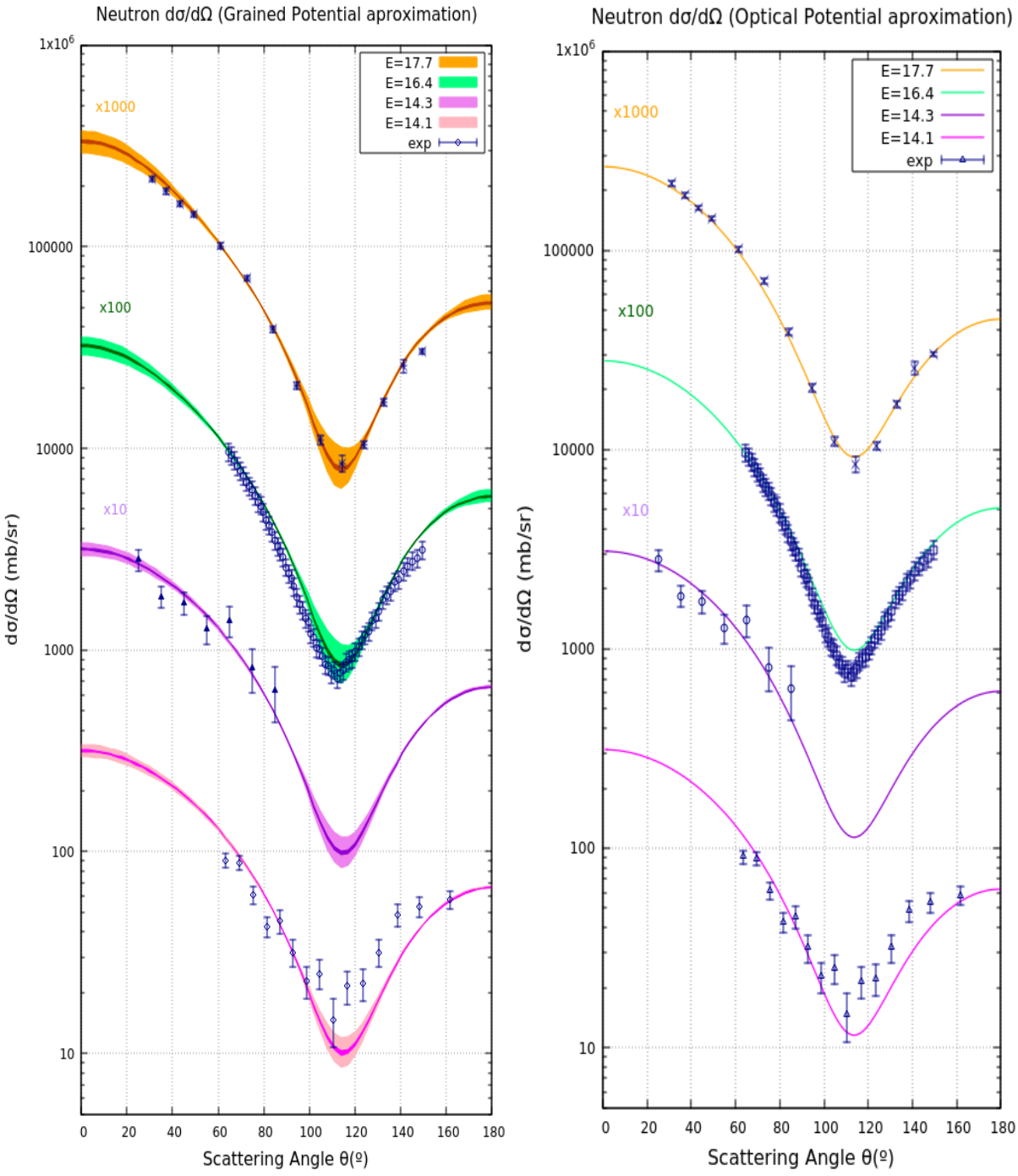

Figure 24: Neutron differential cross section at different energies calculated using the grained potential model with the average parameter values of Table 8. The bands associated to the errors represent the 68% confidence limits. The dark bands have been calculated considering only the most populated branches and the light ones both of them. These values are all re-scaled in accordance with the χ^2 obtained value. (b) Neutron differential cross section computed using the optical potential model. Dark blue points are the experimental differential cross section values.

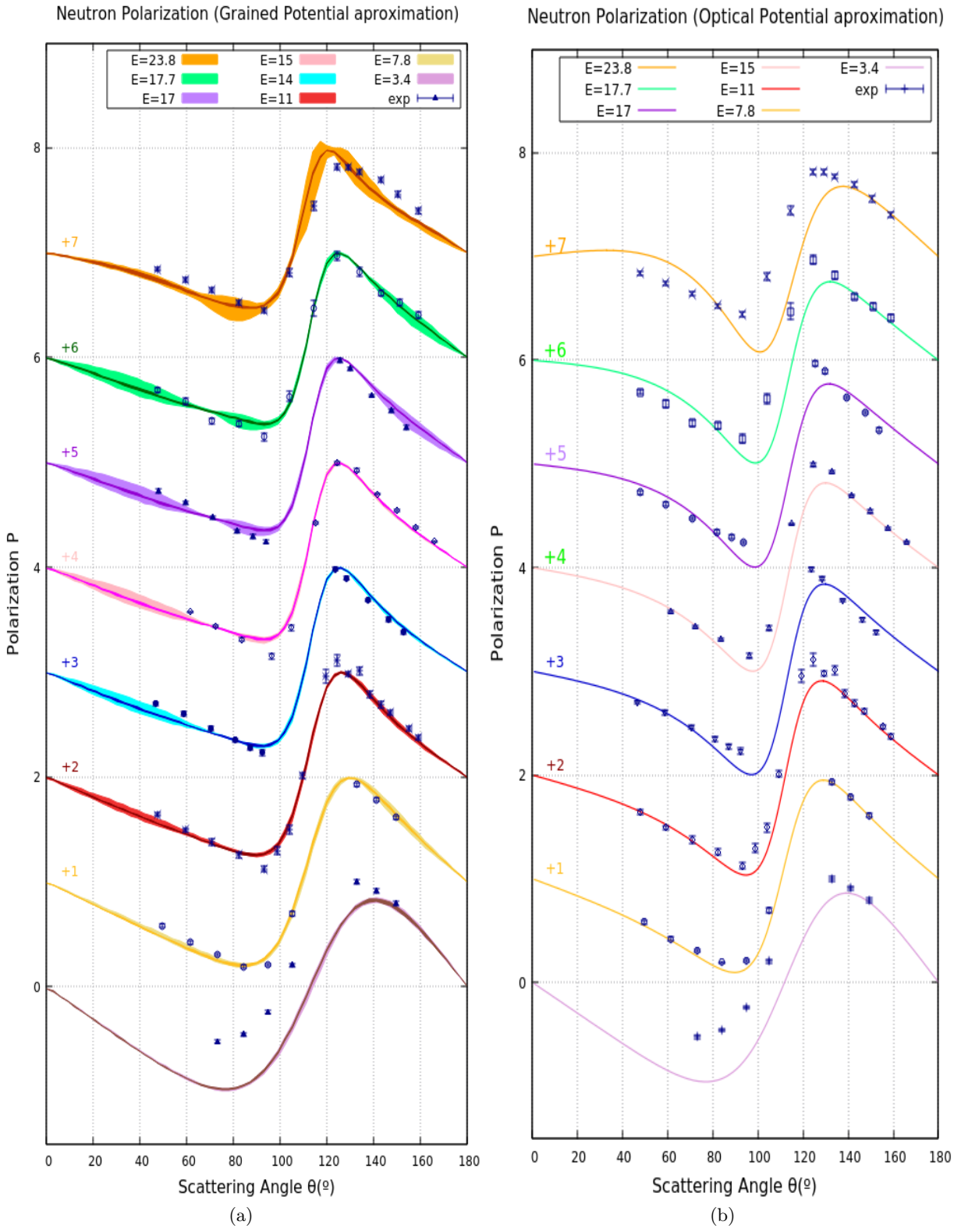

Figure 25: (a) Neutron polarization at different energies calculated using the grained potential model with the average parameter values of Table 8. The bands associated to the errors represent the 68% confidence limits. The dark bands have been calculated considering only the most populated branches and the light ones both of them. These values are all re-scaled in accordance with the χ^2 obtained value. (b) Neutron polarization computed using the optical potential model. Dark blue points are the experimental polarization values.

As we can quickly see, the lowest energies values show the biggest discrepancies. When excluding those 7 data from the minimization, we achieve a much smaller χ^2 value as we will discuss in the next section.

10.4 χ^2 obtained values.

We calculate the χ^2 values first using the first found minimum in Table 7, then using the Bootstrap method the average minimum value of the χ^2 (first found minimum) is obtained for both cases: before the selection of the branch (average obtained minimum), and the one calculated with the new input simplex, rejecting the less populated solution branch (average obtained minimum (2)). Finally, the Bootstrap method has been used excluding the low energy data to calculate the χ^2 value. (Average obtained minimum (3)). To compare our potential method and the optical one we also calculated the χ^2 distribution taking the initial 20 square wells method using potential values predicted by the optical potential. A summary of the χ^2 obtained values and the χ^2 per degree of freedom. $\left(\frac{\chi^2}{\nu}\right)$ is shown in Table 9.

Grained Potential Approximation	χ^2	$\frac{\chi^2}{\nu}$
First found minimum	6567	34
Average obtained minimum	6692	34
Average obtained minimum (2)	6511	34
Average obtained minimum (3)	1534	8

Optical Approximation	χ^2	$\frac{\chi^2}{\nu}$
First χ^2 *calculation*	15564	80
Second χ^2 *calculation*	12072	65

Table 9: χ^2 values obtained for both Grained Potential Approximation and Optical Approximation. First found minimum Table (7), Average obtained minimum (average potential values obtained after the Bootstrap method Table (8) considering all branches), average obtained minimum (2) (calculated considering only the most populated branch) and average obtained minimum (3) (the one calculated excluding low energy data). For Optical Approximation, the first calculation includes all data set and the second one excludes low energy data.

Although lower values have been obtained using the grained potential approximation, the results are not statistically admissible. A theoretical model reproduces the experimental data only if the χ^2 per degree of freedom is $\frac{\chi^2}{\nu} = 1 \pm \sqrt{\frac{2}{\nu}}$.
Two different fitting processes for each set of observables experimental data were also made, obtaining the values shown in Table 10. The χ^2 values obtained for a differential cross section fit excluding polarization data drop dramatically. Polarization is dominating the total fit.

Grained Potential Approximation	χ^2	$\frac{\chi^2}{\nu}$
D. cross section	123	1.4
Polarization	6050	63

Optical Approximation	χ^2	$\frac{\chi^2}{\nu}$
D. cross section	261	2.9
Polarization	11811	123

Table 10: χ^2 Values obtained independently for the two different observables for both grained Potential Approximation and Optical Approximation.

10.5 Re-scaling the confidence intervals

The 68% confidence intervals are the associated obtained errors of a χ^2 distribution. In our study the obtained value for the distribution is far from being the theoretical one $\left\langle \frac{\chi^2}{\nu} \right\rangle = 1$. As suggested in [16] the χ^2 distribution can be re-scaled to have the theoretical value $\left\langle \frac{\chi^2}{\nu} \right\rangle = 1$. To estimate our error we have to re-scale the 68% confidence intervals using the same procedure. They are $\sqrt{\frac{\chi^2}{\nu}}$ times larger than the theory (for $\chi^2 = 1$) predicts.

11 Conclusions and outlook

In this work we have developed mathematically the coarse graining potential method which reproduces successfully previous results obtained by other authors using a continuous function for the interaction potential instead. This method, with a simple underlying theory (sum of several square wells) gives the fitting parameters a physical meaning, they correspond to the depth of such square well set. The number of fitting parameters can be determined beforehand by the knowledge of the energies of the incident particle being such set considerably small. It is not efficient or, in any case, necessary to increase this number because of the uncertainty principle. Additionally, the weight of each parameter to the fitting process can be estimated when selecting a concrete experimental data set since we can associate a classical impact parameter to them. This is useful to know in advance the importance of each parameter in the fit. Also, an analysis of confidence intervals of the results has been carried out with the Bootstrap Monte Carlo simulation, providing us an idea of the errors associated to the method for parameters and observables.

We observe that this model does not reproduce properly the results of low energy data and we have proved that when excluding them, a considerably smaller χ^2 is obtained. In the future some considerations should be taken into account if we want to extend this coarse graining method to the low-energy limit.

In general, for all possible scenarios, we achieve much better χ^2 values with the graining method than other studies, (in general 2.5 times lower values). Nevertheless, the $\left(\frac{\chi^2}{\nu} = 32.6\right)$ value, is far from being a theoretically acceptable value $\left(\frac{\chi^2}{\nu} = 1 \pm \sqrt{\frac{2}{\nu}}\right)$. This is mainly due to the high precision polarization data, which dominate the fit. It could be that the errors predicted for this data are underestimated. When selecting only differential cross section ones the χ^2 value drops dramatically achieving a χ^2 per degree of freedom of $\left(\frac{\chi^2}{\nu} = 1.4\right)$.

With this theoretical model it could be possible to search for experimental discrepancies in large data bases by checking their incompatibility and possibly getting to exclude the ones lying outside the prediction bands. Also in the future this model could be extended and implemented to higher energy ranges taking into account new considerations in the potential, such as the complex and energy dependent character of the optical potential.

References

[1] R.H.Landau Scattering, chp. 1 in *Quantum Mechanics II* 2nd ed. 2004. WILEY-VCH, Weinheim, Germany.

[2] J.R Taylor Introduction, chp. 1 in *Scattering-Theory* 2nd ed. 1972. Jonh Wiley and Sons. Boulder,Colorado

[3] A. Galindo, P. Pascual Scattering Theory, ch. 8 in *Quantum Mechanics II*, 2nd ed. 1990. Springer Verlag, Berlin Heidelberg, Germany.

[4] A. Galindo, P. Pascual Special functions, apendix A en *Quantum Mechanics I*, 2nd ed. 1990. Springer Verlag, Berlin Heidelberg, Germany.

[5] J.R. Taylor The Chi-Squared test for a Distribution, cap. 12 en *An introduction to Error Analysis the study of uncertainties in physical measurements* 2nd ed. 2004. University Science Books, Sausalito, California.

[6] F.S Pedro Interacción neutrón protón en ondas S con potencial óptico granulado hasta 3GeV

[7] G.R Satchler, L.W.Owen,G.L Morgan, R.L Walter (1968) An Optical Model for the Scattering of nucleons from ^4He at energies below 20 MeV, *Nuclear Physics* **A112**,pp.1-31.

[8] E.Smith, R.Woodhouse and Z.Papp (2012) Refinement of the $n-\alpha$ and $p-\alpha$ fish-bone potential, *Physical review C* **86**, pp. 45-60.

[9] B.Hoop,H. H. Barschall Scattering of neutrons by α particles, *Nuclear Physics* **83**,pp 65-79.

[10] I.J.Thompson, A.R. Barnett (1986) Coulomb and Bessel Functions of Complex Arguments and Order, *Journal of Computational Physics* **64**, pp 490-509.

[11] T.H May, R.L. Walter, H.H Barschall(1963) Scattering of Polarized Neutrons by α particles, *Nuclear Physics* **45**, pp 17-26.

[12] R. Navarro Pérez, J.E. Amaro, E. Ruiz Arriola (2014) Partial wave analysis of Chiral NN interactions, *Few-Body Systems* **55**, issue 8-10, pp. 983-987.

[13] R. Navarro Pérez, J.E. Amaro, E. Ruiz Arriola (2012) Coarse graining nuclear interactions, *Progress in Particle and Nuclear Physics* **67**, pp. 339-364.

[14] R. Navarro Pérez, J.E. Amaro, E. Ruiz Arriola (2014) Coarse-grained NN potential with chiral two-pion exchange, *Physical Review C* **89**.

[15] P.Fernández-Soler, E. Ruiz Arriola (2014) Coarse graining of NN inelastic interactions up to 3 GeV: Repulsive versus structural core, *Physical Review C* **96**.

[16] R. Navarro Pérez, J.E. Amaro, E. Ruiz Arriola (2014) Statistical error analysis for phenomenological nucleon-nucleon potentials, *Physical Review C* **89**.

[17] R. Navarro Pérez, J.E. Amaro, E. Ruiz Arriola (2014) Bootstraping the statistical uncertainties of NN scattering data, *Physics Letters B* **155-159**.